Investigation on the mechanism for the aerofoil noise near stall conditions

Giovanni Lacagnina* and Paruchuri Chaitanya

Institute of Sound and Vibration Research, University of Southampton, UK

Tim Berk

Aerodynamics and Flight Mechanics Research Group, University of Southampton, UK

Jung-Hoon Kim

Faculty of Engineering, University of Nottingham, UK

Phillip Joseph

Institute of Sound and Vibration Research, University of Southampton, UK

Bharathram Ganapathisubramani

Aerodynamics and Flight Mechanics Research Group, University of Southampton, UK

Seyed Mohammad Hasheminejad

Department of Mechanical, Aerospace and Civil Engineering, Brunel University, UK

Tze Pei Chong

Department of Mechanical, Aerospace and Civil Engineering, Brunel University, UK

Oksana Stalnov

Technion−Israel Institute of Technology, Haifa, Israel

Kwing-So Choi

Faculty of Engineering, University of Nottingham, UK

Muhammad Farrukh Shahab, Mohammad Omidyeganeh, and Alfredo Pinelli

School of Mathematics, Computer Science and Engineering, City University London, UK

(Dated: October 31, 2019)

Abstract

The main focus of this paper is on investigating the noise produced by an aerofoil at high angles of attack over a range of Reynolds number $Re \approx 2 \cdot 10^5 - 4 \cdot 10^5$. The objective is not modelling this source of noise but rather understanding the mechanisms of generation for surface pressure fluctuations, due to a separated boundary layer, that are then scattered by the trailing edge. To this aim, we use simultaneous noise and surface pressure measurement in addition to velocimetric measurements by means of Hot Wire Anemometry and Time-Resolved Particle Image Velocimetry. Three possible mechanisms for the so-called "separation-stall noise" have been identified in addition to a clear link between far field noise, surface pressure and velocity fields in the noise generation.

I. INTRODUCTION

There are many examples in which an aerofoil operates close to stall, either intentionally to maximise lift, or inadvertently, such as in the case of a wind turbine blade experiencing a sudden gust. Aerofoils operating close to stall generally suffer a degradation in aerodynamic performance. Moreover, at these conditions, aerofoils are also well known to be particularly noisy, characterized by large increases in low frequency noise [1]. This paper is a detailed experimental study into the characteristics and mechanisms of this additional increase in low frequency noise.

Increasing the aerofoil angle of attack produces an increase in the adverse pressure gradient over the aerofoil suction side, which then induces a separation of the boundary layer from the surface. As long as this separation is incipient, the separated layer is still able to reattach to the surface in a relatively short distance. In some cases, reattachment can occur in less than 1% of the chord [2]. Increasing the incidence angle further causes the point of reattachment to move further downstream. Transition may occur near this reattachment point, triggering the onset of a turbulent boundary layer that convects past the trailing edge and then scatters into sound. In general, if the flow conditions change from laminar to turbulent, the size of the separated wake can be reduced and the onset of separation can be delayed since the energizing effect of the outer layer on the turbulent boundary layer is greater than in the laminar case due to the turbulent mixing motion [3]. In a general situation, where the turbulence is generated within the aerofoil boundary layer itself and then interacts with the trailing edge to generate noise, the noise generation mechanism is well

* G.Lacagnina@soton.ac.uk

understood and can be predicted with reasonable accuracy using classical flat plate theory once the boundary layer pressure statistics are known near the trailing edge [4]. Once the boundary layer becomes separated from the trailing edge there is evidence that the radiated noise can still be determined from the pressure statistics close to the trailing edge [5]. However, the cause of these pressure fluctuations are much less well understood. This paper provides further evidence that the noise radiated under near-stall conditions arises from trailing edge scattering. However, its main focus is to investigate the cause of these pressure fluctuations, which has received comparatively little attention in the literature.

A. Previous work

Aerofoil separation noise is one example of a class of aerofoil noise generating mechanisms, categorised as aerofoil self-noise, in which (predominantly) hydrodynamic pressure fluctuations convect over the trailing edge, identified by Brooks et al. in 1989 [1]. Separation noise is characterised by a significant increase (typically more than 10 dB ([6])) in low frequency noise ([7]) relative to the noise at low angles of attack, when the boundary layer is attached.

Aerofoil noise at near-stall conditions has been measured in a number of studies ([1, 5, 8–10]). These measurements have been used to develop models of the radiated noise. The best known of these has arisen from the empirical BPM model ([1]) by Brooks et al, which provides predictions of the radiated noise at 90° to the trailing of a NACA0012 aerofoil over a range of angles of attack, including stall conditions. The main input parameters to this model are the displacement and boundary layer thicknesses at the trailing edge, which are also determined from empirical expressions. We note, however, that the notion of boundary layer thickness is less well defined for a separated shear layer. The implicit assumption, therefore, is that the noise spectrum is completely determined by eddy structures within the separated flow, whose size is determined by the boundary layer thickness. According to Brooks et al ([1]) the contribution to the total noise due to the separated portion of the turbulent boundary layer on the suction side, based on the suction side boundary layer thickness, is predicted by the formula:

$$SPL_\alpha = 10log\left(\frac{\delta_s^* M^5 L \overline{D}_h}{r_e^2}\right) + B\left(\frac{St_s}{St_2}\right) + K_2$$

where δ_s^* is the displacement thickness on the suction side, M is the Mach number, L is the spanwise extent wetted by the flow (aerofoil width), $\overline{D}_h$ is a directivity function, r_e is the retarded

observer distance, B is the spectral shape function, which depends on the Strouhal number based on the displacement thickness on the suction side ($St_s = \frac{f\delta_s^*}{U}$) and on the peak Strouhal number St_2 where the trailing edge noise is maximum, and K_2 is an amplitude function, depending on the angle of attack and Mach number. More details about the model can be found in the paper [1].

Moreau et al. [8] have developed an analytical model for predicting aerofoil separation noise. It is based on experimental measurements of the wall pressure spectra and spanwise coherence lengths for NACA0012 and NACA65-(12)10 aerofoils. More recently, Schuele and Rossignol ([9]) have proposed a model based on the TNO-Blake formulation in which the surface pressure fluctuations are determined from the steady and unsteady boundary layer velocity statistics via the solution to Poisson's equations for incompressible flow. The model was used to determine the radiated noise due to the separated boundary layer of a DU-96-W-180 aerofoil. It was shown to achieve good levels of agreement with experimental data in the mid-frequency range. Suryadi and Herr ([10]) have extended the study on the same aerofoil in order to better predict the low frequency range by means of a modification of the correlation lengths. Finally Bertagnolio et al. ([5]) have developed an empirical model for the surface pressure spectrum, based on a series of curve fittings of the surface pressure spectra data obtained from many different aerofoil profiles and Reynolds numbers. This model only requires the separation point location as an input parameter and was shown to provide predictions that are in good agreement with various noise measurements. However, some discrepancies were observed in the low frequency range for some particular configurations. The precise range of frequencies for which separation noise is most prominent depends on the physical extent of the separated area, which is a strong function of the chord length. For example, as reported by Moreau et al [8], the noise associated with stall conditions for an aerofoil of chord length c = 0.15 m is in the range of frequencies ($f \approx 10^2 - 10^3$ Hz). Further evidence of the importance of the chord length for separation noise can be found in Paterson et al. ([7]), who found significant levels of correlation between far-field and surface pressure microphones. They estimated the cross-correlation zero-crossing time delay amongst far field and surface pressure microphones. For moderate angles of attack, this time delay monotonically decreases moving the surface pressure sensor location downstream along the chord approaching the trailing edge. This is an evidence of noise produced in correspondence to the trailing edge. In deep stall conditions, they have shown that, once you get closer to the trailing edge, this time delay starts reducing less, so that the related estimate of convective velocity of disturbances results in a very high value, higher than the free stream velocity. This is unlikely and suggests that the noise

production process occurs also upstream of the trailing edge (allowing a different distance over which should be estimated the convective velocity, given the time delay), so that the dimension of the aerofoil, and its chord, are now relevant for the noise generation. However, whilst the previously described models establish the link between the surface pressure near the trailing edge, due to hydrodynamic pressure fluctuations, and the far field acoustic radiation, none of these studies have elucidated the mechanism of surface pressure fluctuations due to a separated boundary layer. This is the main objective of the current paper.

B. Objectives and scope of the paper

This paper is a detailed investigation into the relationship between velocity fluctuations in the boundary layer and shear layer, the surface pressure fluctuations near the trailing edge and the far field noise due to the NACA-65 family of aerofoils over a wide range of angles of attack, including pre and post stall conditions. Simultaneous far field and surface pressure measurements were made in order to establish the link between them. Time Resolved Particle Image Velocimetry (TRPIV) and Hot Wire Anemometry (HWA) were also used in combination with the unsteady surface pressure measurements in order to understand the mechanisms of separation/stall noise on aerofoils. The Reynolds number (Re) for the current study is in the range $Re \approx 2 \cdot 10^5 - 4 \cdot 10^5$.

This paper is organised as follows: In section II the possible separation/stall noise generation mechanisms are reviewed. The aerofoil geometry is described in section III, and the experimental setup and measurement techniques are described in section IV. In section V far field noise, unsteady surface pressure and the velocity field measurements are presented and their interrelationships discussed. Conclusions and a summary of the main findings are presented in Section VI.

II. SEPARATION NOISE MECHANISMS

A separated flow developing over an aerofoil surface is a complex phenomenon, which may involve a transition to a fully turbulent flow and the occurrence of instabilities and shed vorticity. Two distinct flow regimes can be identified: the free stream, where the velocity is close to the undisturbed state, and a separating boundary layer region, involving flow recirculation. These two zones are separated by a shear layer which is prone to being unstable and rolling up to form vortices

([11]). The characteristics of these vortices can depend on the static surface pressure distribution over the aerofoil which generally depends on geometry, Reynolds number and angle of attack ([11, 12]). Based on elementary considerations of the dynamics of separating shear layers, three possible distinct noise generation mechanisms can be identified:

1. *Coherent structures convected in the detached shear layer.*

   When a separated flow is developing over an aerofoil, a span-wise vortex roll-up process of the separated shear layer is triggered [13]. This generates vortex structures oriented in the span-wise direction that while convected downstream tend to break down and tilt towards the streamwise direction [14] The transit of these coherent structures in the shear layer passing over the trailing edge will induce an unsteady hydrodynamic pressure over the aerofoil surface, which then scatters at the trailing edge and radiates to the far field (Figure 1 a). In a recent paper by Berk et al. ([15]), PIV velocity data of the flow field were combined with simultaneous measurements of the surface pressure on a NACA0012 aerofoil to demonstrate the causal link between instances of high (or low) pressure on the surface with coherent structures passing over the trailing edge. A similar procedure will be adopted here to demonstrate the existence of coherent structures in the shear layer and their link to the far field radiation due to a NACA65 aerofoil at high angle of attack.

2. *Instabilities in the detached shear layer*

   Wave-like instabilities, such as Kelvin-Helmholtz instabilities [16], can occur in the separated shear layer (Figure 1 b). Such waves have been shown to be theoretically possible from unstable solutions of the Orr Sommerfield equation, whose eigenfrequencies have been shown to closely correspond with peaks in the hydrodynamic pressure spectrum on the aerofoil surface [17]. These largely convected modes will induce surface pressure fluctuations on the surface and subsequently radiate as sound.

3. *Shear layer flapping*

   In conditions of incipient separation, it has been found ([18, 19]) that the shear layer can exhibit a flapping motion (Figure 1 c). This is generally found to be a low frequency phenomenon, usually occurring at a non-dimensional frequency of $(St \approx 0.02 - 0.03)$, where the Strouhal number is defined as $St = \frac{f\,c\,sin(\alpha)}{U_\infty}$, based on the projected width obstructing the flow (i.e. $c \cdot sin(\alpha)$), where c is the aerofoil chord and α is the angle of attack. The

flapping phenomenon is associated with a periodic switching between stalled and unstalled conditions downstream to the leading edge. Evidence for flapping as a low frequency noise phenomenon is presented below in Section V I.

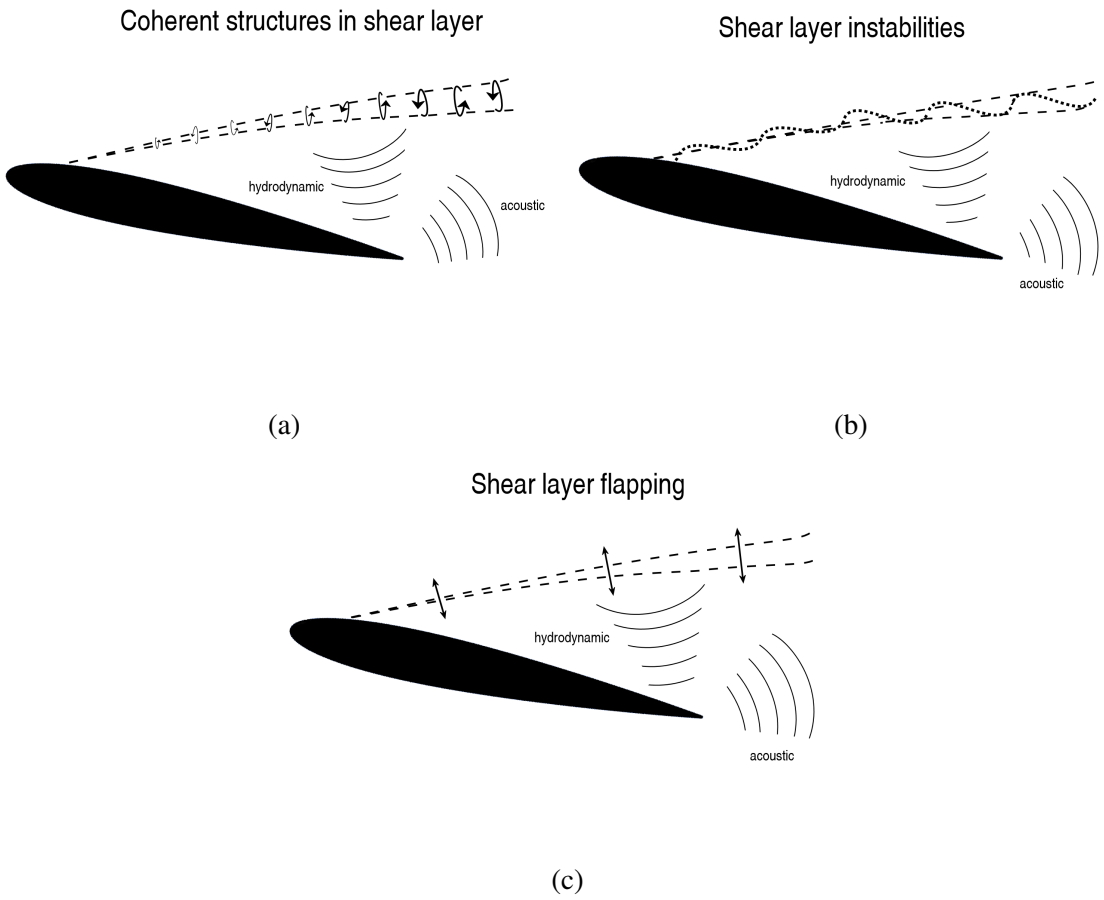

FIG. 1: Possible separation noise mechanisms associated to a) coherent structures in the shear layer; b) shear layer instabilities; c) shear layer flapping

III. AEROFOIL CONFIGURATIONS

The experimental investigation of aerofoil stall noise presented in this paper is based on the NACA65-(12)10 family of aerofoils, which are high-performance aerofoils, designed to maximize the region of laminar flow over their surface ([20]). They are often used in cascades and turbines. The NACA65-(12)10 aerofoil under investigation has a chord of 0.15 m and a span of 0.35 m. To avoid possible tonal noise generation due to Tollmien - Schlichting instabilities, occurring when the aerofoil is in a laminar condition, the flow near the leading edge was tripped by means of a

band of sandpaper at a location of around one third of the chord (5 cm) from the leading edge on both the pressure and the suction sides. The sandpaper covered the entire span of the aerofoil and had a thickness t = 0.5 mm and a width in the stream-wise direction w = 1 cm.

IV. EXPERIMENTAL SETUP

A. Facility

All noise and flow measurements were performed in the open jet wind tunnel facility at the Institute of Sound and Vibration Research (ISVR), at the University of Southampton. Photographs of the facility and the experimental set up are shown in figures 2. A detailed description of the wind tunnel can be found in Chong et al [21]. It is housed inside the university's large anechoic chamber, with dimensions of 8 m x 8 m x 8 m, whose walls are acoustically treated with glass wool wedges whose cut-off frequencies are 80 Hz. The nozzle dimensions are 0.5 m in height and 0.35 m in width. This height of nozzle together with the chord length of 0.15 m, ensures that the downwash deflection of the jet is sufficiently small to readily allow measurements at post-stall conditions. The ratio between the geometrical angle α_{geom} and the effective angle of attack α_{eff}, i.e. after flow deflection has been taken into account, can be estimated from the relationship derived by Brooks et al [22], which applied to the current configuration is:

$$\zeta = \frac{\alpha_{geom}}{\alpha_{eff}} \approx 1.5$$

where $\zeta = (1+2\sigma)^2 + \sqrt{12\sigma}$, $\sigma = (\frac{\pi^2}{48}\frac{c}{H})^2$, c the aerofoil chord and H the nozzle height. The aerofoil is held in place by two side plates, which also maintain the two-dimensionality of the flow, attached to the side walls of the nozzle. The leading edge of the aerofoil was 0.15 m (one chord) downstream of the nozzle lip.

The velocity for all the measurements was set to a value of 20 m/s or 40 m/s corresponding to a value of Reynolds number (Re) $Re \approx 2 \cdot 10^5$ and $Re \approx 4 \cdot 10^5$.

B. Noise measurement

Noise measurements were made using a polar array of ten half-inch condenser microphones (*B&K* type 4189), located at a distance of 1.2 m from the trailing edge at the mid span plane of

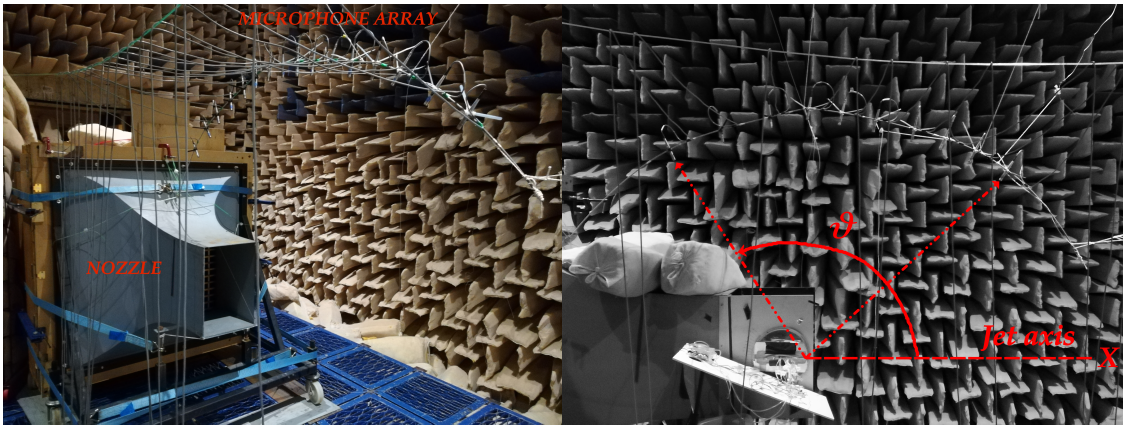

(a) (b)

FIG. 2: Left) Open wind tunnel and acoustic setup inside the ISVR's anechoic chamber; Right) Microphones emission angles

the aerofoil, as shown in figure 2 Right. The microphones emission angles range from 40 to 130°, relative to the aerofoil trailing edge and downstream direction of the jet axis. Measurements were made at a sampling frequency of 40 kHz for a duration of 20 s. The total number of samples is then $8 \cdot 10^{-5}$ and the PSD estimate window length is 4096 samples. This combination of parameters gives a frequency resolution Δf of 1/0.1024 = 9.8 Hz. The normalised variance of the spectral estimate is equal to $\frac{1}{2\Delta f T}$, where $\Delta f\, T$ is the so-called 'BT-product'. For this combination of parameters the normalised variance of the spectral estimate is therefore 0.003, which is negligible.

C. Steady and Unsteady pressure on aerofoil surface

Pressure measurements on the aerofoil surface where made via a number of capillary tubes that run below the aerofoil surface between pressure taps, along the aerofoil chord and along the span close to the trailing edge, and a number of T-junctions connected to miniature microphones. More specific information about the arrangement of pressure taps and tubes can be found in section V B The microphones are 2.5 mm diameter omnidirectional electret condenser microphones (Knowles Electronics 206 FG-3329-P07). On the other side of the T-junction are capillary tubes approximately 3 m in length to avoid reflections. Surface pressure measurements were also acquired simultaneously to the far field noise for a duration of 20 s at a sampling frequency of 40 kHz. The total number of samples is then $8 \cdot 10^{-5}$ and, given the same PSD window length as

for the noise measurements, similar observations about the variance of the spectral estimate can be made. Special care was given to the sealing of the microphone within the block, which was found to affect the pressure measurements. The miniature microphones were calibrated in-situ against a reference *B&K* $\frac{1}{4}$ *inch* condenser microphone by means of an in-duct loudspeaker. This arrangement of capillary tubes was also used to measure the steady pressure coefficient C_p, by replacing the microphones with membrane-based piezo-resistive amplified pressure sensors (First Sensor HCLA0050) having an operating pressure in the range $0 \pm 50\,mbar$ with a ratiometric analog output signal.

D. PIV measurement

The steady and unsteady velocity fields around the aerofoil at angles of attack close to stall were investigated by means of Time Resolved Particle Image Velocimetry (TRPIV) at a frequency of 4 kHz and based on the acquisition of roughly 20,000 images, corresponding to 5 s of data, by means of the setup shown in the photograph in Figure 3 (Left). A Nd:YLF laser capable of a high-repetition rate of up to 10 kHz was used to generate a light beam which was then converted by a system of cylindrical and spherical lenses into a light sheet of 1 mm thickness with which to illuminate the vertical plane along the chord of the aerofoil in the streamwise direction. Two high speed Phantom v641 cameras, set at a resolution of 1024 x 512 pixels (0.5 MP), were used to frame the area around the aerofoil, mostly on the suction side, in a T-shape configuration, see figure 3 (Right). The cameras have a 10 μm sensor pixel size and are equipped with an 85 mm focal length lens. The flow was seeded using a Martin Magnum 1200 smoke machine located at the inlet of the centrifugal fan of the wind tunnel, which provided a uniform particle distribution of the flow from the nozzle with diameters of roughly 1 μm. The average particle image size was approximately 2.2 pixels and the number of particles per pixel (N_{ppp}) was about 0.038, which is close to the optimal value prescribed by Willert and Gharib of $(N_{ppp} = 0.035)$ [23] and in agreement with the recommendations of Raffel et al. [24] and Cierpka et al. [25] $(0.03 < N_{ppp} < 0.05)$. Finally, the magnification factor M was about 6.7 pixel/mm (roughly 0.15 mm/pixel). The calibration between the object domain and the image domain was performed using the recommended procedure described in Adrian and Westerweel [26]. The PIV images were processed using digital cross-correlation analysis (Willert and Gharib [23]). A multi-grid/multi-pass algorithm (Soria [27]), with an iterative image deformation (Scarano [28]; Huang et al [29];

Jambunatan et al. [30]; Nogueira et al. [31]) was used to compute the instantaneous velocity fields having a final interrogation window size of 32x32 pixels with an overlap factor of 75%. In order to eliminate spurious vectors, a vector validation algorithm, based on a regional median filter (Westerweel and Scarano [32]), with a kernel region of 3 x 3 vectors, and group removing, was applied.

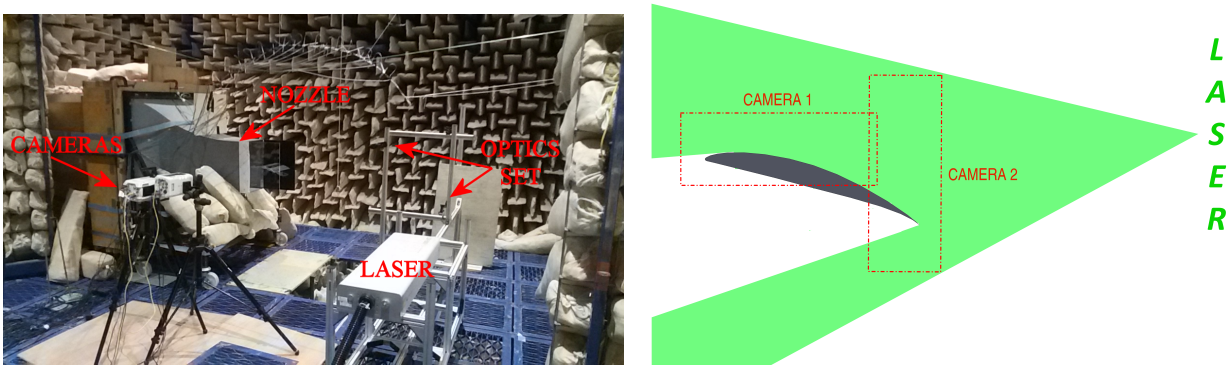

(a) (b)

FIG. 3: Left) TRPIV setup inside the ISVR's anechoic chamber; Right) Sketch showing the PIV cameras fields-of-view (dashed lines) and the total framed area.

V. RESULTS

A. Validation of measurement procedure

By way of validation of the measurement procedure and of the wind tunnel, initial measurements were made of the noise due to a NACA0012 aerofoil of 0.2 m chord at high angle of attack and compared against the spectra predicted by the model due to Brooks et al [1], which provides estimates for the 1/3-octave band frequency spectrum for the different "self-noise" mechanisms, including separation noise, associated to a NACA0012 aerofoil. Figure 4 shows the comparison between the measured and predicted sound pressure level spectra at a location 90° from the trailing edge, a free stream velocity equal to $U_\infty = 20$ m/s, and an effective angle of attack of $\alpha_{eff} = 12°$, for which separation noise was found to be the dominant noise mechanism in the mid-frequency range. The experimental noise spectral density is integrated over a bin width of 4.9 Hz. In this figure both the predicted overall noise and separation noise alone are plotted. The spectral hump due to separation predicted by Brooks et al. can be clearly observed in the measured spectrum

in the frequency range between about 250 Hz and 1500 Hz. Below this frequency the measured spectra is dominated by facility noise. The reason for the discrepancy above 1500 Hz is not clear. Nevertheless, the level of agreement in the region of the spectral hump is sufficient to validate the measurement procedure and facility. We now investigate the characteristics of separation noise due to a different aerofoil, the NACA65-(12)10, at a flow speed of 40m/s.

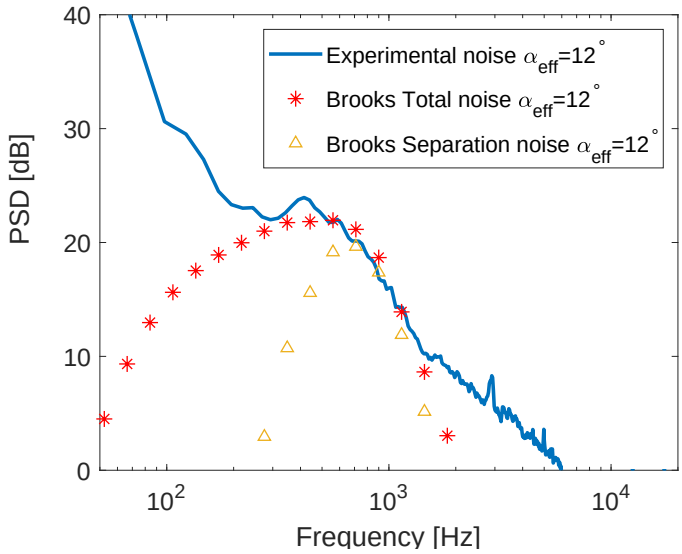

FIG. 4: Measured NACA0012 noise spectra vs Brooks et al. [1] predicted total self-noise and separation noise contribution at $\alpha_{eff} = 12°$

B. Steady pressure on aerofoil surface

Before investigating the characteristics of the radiation from the NACA65-(12)10 aerofoil at high angle of attack, we first assess the steady pressure coefficient C_p distribution along the mid-chord in order to determine the development of the separated flow areas and hence determine the angle of attack at which stall conditions are established. The C_p distribution was estimated from just five pressure taps along each of the pressure and suction sides of the aerofoil chord, evenly distributed between 15 mm from the leading edge and 5 mm from the trailing edge. By way of validation of the measurement technique and to assess the accuracy of the pressure sensors, we have compared the measured C_p with the one obtained from XFoil ([33]) but only for the range of angles at which XFoil gives a converged solution $\alpha \leq 10°$. The comparison is shown in figure 5 and the agreement is good both in terms of shape and identification of flow separated regions (see

$\alpha = 10°$) as the region of nearly constant static pressure [34]. Figure 5 b shows now the measured C_p only and, since the separation mainly occurs on the aerofoil suction side, only C_p on this side is shown in this figure for some representative angles of attack.

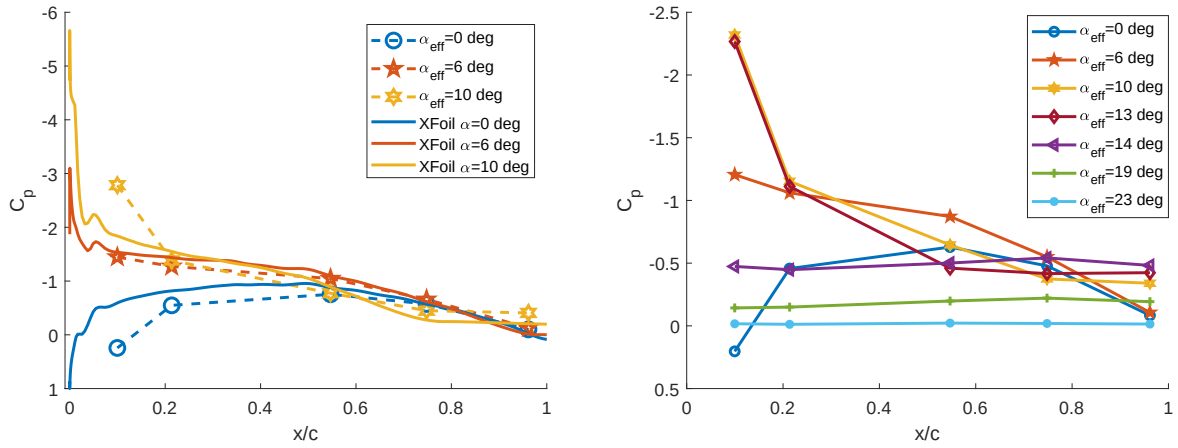

(a) (b)

FIG. 5: NACA65(12)10 aerofoil suction side: Left) Comparison between the pressure distribution measured by pressure sensors and estimated by XFoil; Right) Measured pressure distribution at different angles of attack. $U_\infty = 40$.

At moderate angles of attack ($\alpha_{eff} = 0° - 6°$), the flow can be seen to remain attached over the entire aerofoil surface. At the angle of attack of $\alpha_{eff} = 10°$, a separated flow area is established close to the TE of the aerofoil (the final 20 to 25% of the chord). At $\alpha_{eff} = 13°$, at least 50% of the chord can be seen to be affected, while further increasing the angle of attack to $\alpha_{eff} = 14°$ causes the flow to become separated over the entire suction side surface, eventually becoming fully stalled at angles greater ($\alpha_{eff} = 19° - 23°$). A progressive and gradual upstream movement of the point of separation from the trailing edge towards the leading edge as α_{eff} is increased is usually classified as *trailing-edge stall*, see [35]. A trailing-edge stall generates a "soft" stall marked by a gradual 'bending-over' of the lift-curve at maximum lift, as compared to the sharp, steep drop in C_L for a leading-edge stall ([35]).

C. Characterization of noise spectra

Having made an initial assessment of the different flow conditions around the NACA65-(12)10 aerofoil, we now consider how the radiated noise varies for these different flow regimes. The sound

power level spectra PWL(f) obtained by summing the pressure spectra across the microphones and assuming cylindrical radiation, according to the procedure discussed in [36], was determined for different effective angles of attack in the range $[0^\circ : 26^\circ]$. The noise spectral densities are integrated over a bin width of 4.9 Hz. For the sake of clarity, however, only the angles 0, 6, 10, 13, 14, 19 and 23° are shown in figure 6. For the range of angles of attack corresponding to fully attached flow over the suction side surface, $(\alpha_{eff} = 0^\circ - 6^\circ)$ (as shown from the pressure distribution in figure 5), relatively small increases in noise can be observed with increasing angles of attack. At $\alpha_{eff} = 10^\circ$, where separation at the trailing edge begins to occur, a sudden increase in noise is observed with a peak frequency of about f = 500 Hz. Further increasing the angle of attack to $\alpha_{eff} = 13^\circ$ and $\alpha_{eff} = 14^\circ$ causes an additional and significant increase in noise over a lower frequency range. At $\alpha_{eff} = 19^\circ$ and above, the aerofoil is fully stalled and the maximum noise level decreases but its frequency bandwidth increases.

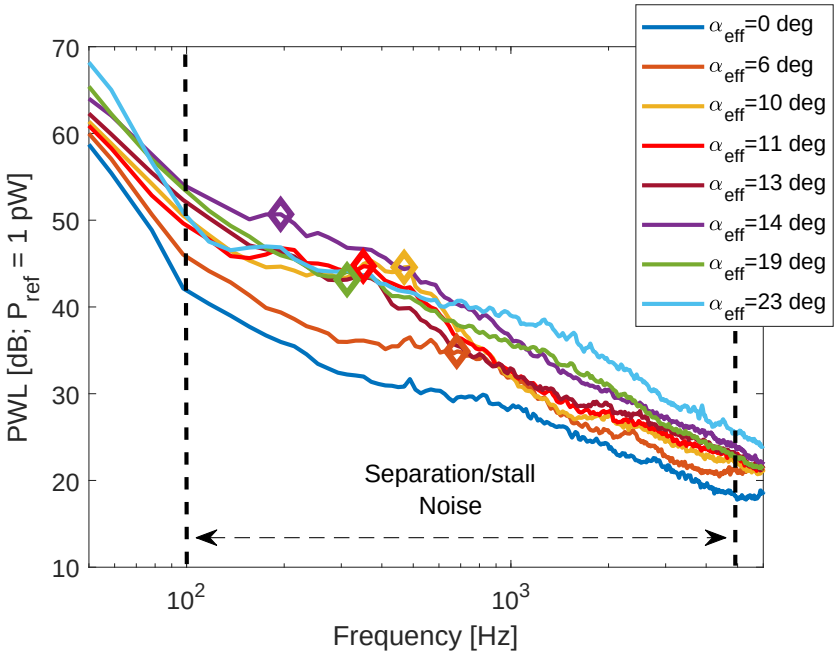

FIG. 6: Noise results for the NACA65(12)10 aerofoil at $U_\infty = 40$ m/s: Sound Power Level at different angles of attack. The figure contains the locations of the center frequencies of the spectral humps as the angle of attack changes from $\alpha_{eff} = 0^\circ$ to $\alpha_{eff} = 14^\circ$. The reference power is $P_{ref} = 1pW$.

For angles of attack higher than $\alpha_{eff} = 6^\circ$, the center frequency of the spectral hump can be observed to reduce as angle of attack increases, while the flow separated region increases its

extension moving from the trailing edge towards the leading edge. This is consistent with the model due to Brooks et al. [1], who predicts the peak frequency based on Strouhal number defined with respect to the boundary layer thickness, or rather the extension of the flow separated region. These peak frequencies are highlighted by markers in figure 6.

A clearer representation of the behaviour of the radiated noise with angle of attack can be seen in figure 7 which shows the variation in sound pressure level versus frequency and angle of attack relative to the noise at 0°. Four different regimes can be clearly identified. These are as follows:

I Low angle of attack, $\alpha_{eff} < 8°$. The flow is still attached at the trailing edge, such that increasing angle of attack causes the boundary layer to become thicker, more energetic and the noise spectrum to shift towards lower frequencies. In this range of angles the relative noise spectrum is nearly flat.

II Mid angles of attack, $8° < \alpha_{eff} < 14°$. The flow separates from the trailing edge and the noise spectrum is concentrated over a relatively narrow frequency bandwidth, which is between about 100 Hz and 800 Hz in this case. In this range of angles the noise appears to be relatively insensitive to angle of attack.

III Critical angle of attack, $\alpha_{eff} = 14°$. At this critical angle the point of separation has just reached the leading edge. At this condition the shear layer turbulence above the trailing edge is highest whilst the height of the shear layer above the trailing edge is lowest. This combination of conditions leads to maximum noise noise generation over the entire frequency range associated to the separation/stall noise while there is a relative noise reduction at high frequencies.

IV High angles of attack, $\alpha_{eff} > 14°$. The flow is stalled on the entire aerofoil suction side. Whilst the shear layer turbulence increases with increasing angle of attack the distance of the shear layer from the trailing edge also increases. Since it is well known that the hydrodynamic pressures generated in the shear layer fall off exponentially with distance, e.g. see the TNO-Blake model [37–39], the noise generation begins to fall with increasing angle of attack. This decrease is limited only by the flow approaching a condition similar to a bluff body as the angles of attack become extremely high.

Based on the previous different regimes, a distinction can be made between:

- *separation noise*: characterised by an unsteady flow close to the surface and for which the noise increase is restricted to a relatively narrow frequency bandwidth with a spectral hump whose center frequency can be associated to the thickness of the separated layer.
- *stall noise*: characterised by an unsteady flow which is farther from the surface and radiates hydrodynamic waves that interact with the body and for which the noise increase broadens to a wide range of frequencies.

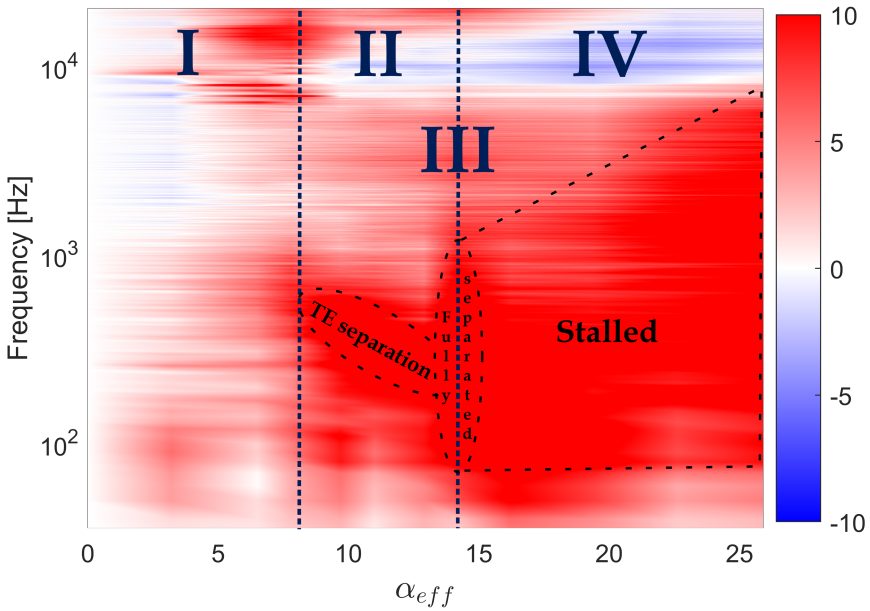

FIG. 7: Noise increase with the angle of attack compared to $\alpha_{eff} = 0°$ for the NACA65(12)10 aerofoil at $U_\infty = 40$ m/s; four different zones are highlighted: Turbulent Boundary Layer (TBL) noise (low angle of attack) (I); Flow separated noise (II); Critical angle $\alpha_{eff} = 14°$ (III); Flow stalled noise (IV)

1. *Relationship between separation noise and lift*

The previous section has demonstrated a close relationship between aerofoil noise at any arbitrary angle of attack and the "state" of the boundary layer. It is therefore reasonable to assume that the variation in overall noise and total lift on the aerofoil with angle of attack follow similar trends. Figure 8 Left shows a comparison between the increase in overall noise from $\alpha_{eff} = 0°$ (left hand scale) and the lift coefficient (right hand scale) versus effective angle of attack. The overall noise

was calculated over a bandwidth of between 10^2 Hz and $5 \cdot 10^3$ Hz and the lift measured on the same aerofoil model by means of 3-component force transducer (Kyowa, LSM-B-SA1, Rated Capacity: 10 N) in the open type wind tunnel at the University of Nottingham with a sampling rate of 0.5 kHz. The frequency bandwidth for the noise was chosen to correspond to the full range of frequency associated to the separation noise (more restricted to low frequency) and stall noise (more broadband). Also shown in this figure are the angles of attack identified in Section V C delineating the four regions of behaviour.

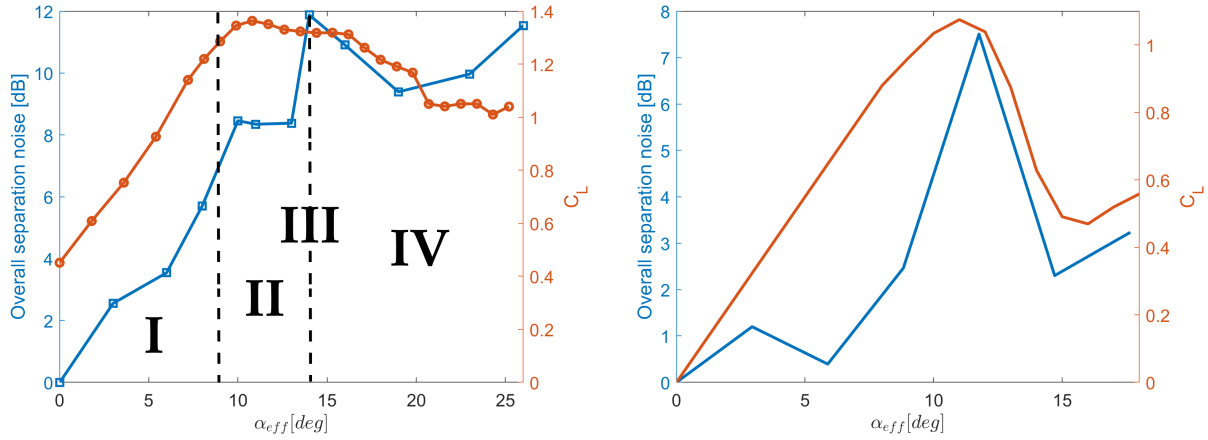

(a) (b)

FIG. 8: Noise results at $U_\infty = 40$ m/s: Trend of the separation noise contribution to the overall noise at different angles of attack vs Lift curve from pressure distribution. a) NACA65 b) NACA0012

Similar variations in lift and overall noise versus angle of attack can be observed. In region I both noise and lift increase with increasing angle of attack. Separation from the trailing edge occurring in region II limits the increase in lift with increasing angle of attack and the overall noise remains roughly constant. At the critical angle in region III, a sharp peak in the noise can be observed corresponding to the angle at which the flow just becomes separated at the leading edge and overall lift begins to reduce. Finally in region IV both noise and lift begin to reduce with increasing angle of attack as the flow becomes increasing detached from the trailing edge. At extremely high angles of attack $\alpha_{eff} > 20^\circ$ the lift and the emitted noise start increasing again. This can be associated to the aerofoil being approached by the flow basically as a bluff body.

Figure 8 provides strong evidence for the close association between lift and overall noise for the NACA65 aerofoil over a wide range of angle attack. It also identifies the condition of maximum

noise. To assess the generality of these findings an identical analysis was performed on the noise and lift data for a NACA0012 aerofoil and the comparison shown in Figure 8 Right. The lift data were taken from the report by Sheldahl and Klimas (1981) [40], choosing the dataset associated to the Reynolds number ($Re = 7 \cdot 10^5$) closest to our current one.

With the scales chosen appropriately the variation in overall noise and lift with angle of attack are in close agreement. In the case of the NACA0012 aerofoil the stall behaviour is more complex since this aerofoil geometry exhibits a trailing edge stall at all Reynolds numbers but a combined leading edge/trailing edge stall at intermediate Reynolds numbers (possibly between $Re \approx 3 * 10^4$ and $Re \approx 3 * 10^6$ [41]), when the aerofoil starts to stall with a turbulent boundary layer moving upstream from the trailing edge but the flow breakdown is completed by an existing laminar separation zone in the leading edge failing to reattach [41]. This is characterized by a "semirounded" lift-curve peak followed by a relatively rapid decrease in lift [42]. Accordingly, the variation in noise and lift around the peak is now much sharper than in the case of the NACA65 aerofoil, which has a much more gentle post-stall behaviour.

D. Simultaneous far field and surface pressure measurements

It is now well established that when the boundary layer is attached at the trailing edge, the far field pressure spectra S_{pp} and hydrodynamic surface pressure spectrum S_{qq} close to the trailing edge are proportional to within a factor of the coherence length $l_y(\omega)$ [4]. In this case, therefore, the trailing edge is the origin of the far field radiation. However, once the flow becomes separated at the trailing edge, it is no longer clear that the far field noise originates from the trailing edge and that this relationship is still valid.

In this section we present simultaneous measurements of the surface pressure and far field noise spectrum over a range of angles of attack. The frequency range over which their spectral shapes are similar therefore corresponds to the range at which the trailing edge is the source of noise. We first present the coherence between them to identify the frequency range over which the far field radiation at a single point is causally related to the surface pressure at a single point on the trailing edge.

Figure 9 (left) shows the coherence between the pressure measured at the pressure tap on the aerofoil suction side closest to the trailing edge (5 mm upstream), and a point in the far field. At the two low angles of attack of 0° and 6°, the coherence between the surface pressure and far

field pressure is negligible over the entire frequency range. The reason for this poor coherence is because the eddy size, which scales on the boundary layer thickness, is much smaller than the aerofoil span. The far-field noise is therefore due to a large number of these small scale eddies interacting with the trailing edge. At 10°, a small hump in the coherence spectrum at about 500 Hz can be observed with a maximum coherence of about 0.2. At 13° the 'hump' now peaks at a value of 0.4 and occurs at the low frequency of about 250 Hz. At much higher angles of attack of 14, 16 and 19°, the peak frequency is now shifted to the much lower frequencies of about 50 Hz. Since in these conditions the noise increase is over a much broader frequency range, as shown in figure 7, it can be speculated that the trailing edge is no more the only source of noise for a fully separated/stalled aerofoil. This conclusion was also reached in the classic paper by Paterson et al. [7] who, by measuring the time delay between the far field noise and different microphones along the chord, showed that the noise at high angle of attack originates somewhere upstream of the trailing edge.

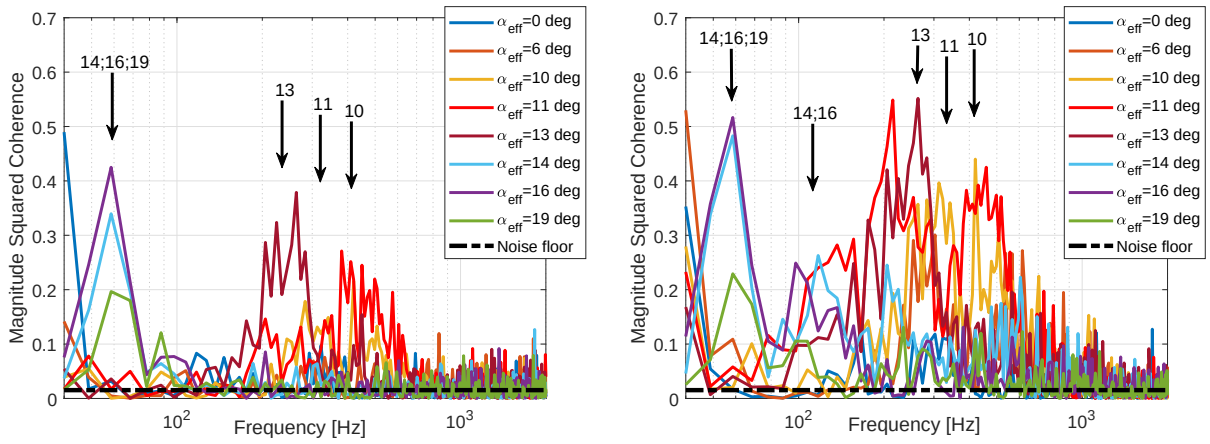

(a) Suction side

(b) Pressure Side

FIG. 9: Coherence between far field noise and surface pressure at TE for the NACA65(12)10 aerofoil at different angles of attack and $U_\infty = 40m/s$ on a) Suction Side b) Pressure side; The dashed lines in a) and b) represent the statistical noise floor; The windowing was 4096 data-points.

E. Estimation of size of 'flow structures' from coherence value

At any flow condition, the far field noise at a single frequency is due to a number of similar flow structures of approximate average spanwise length $l_y(\omega)$ passing over the trailing edge, where $l_y(\omega)$ is the frequency-dependent spanwise coherence length $l_y(\omega) = \int_{-\infty}^{\infty} \gamma^2_{p_s p_s}(\omega, \Delta r) d(\Delta r)$, where $\gamma^2_{p_s p_s}(\omega, \Delta r)$ is the spanwise coherence between the surface pressures separated by a spanwise distance Δr close to the trailing edge. For an aerofoil of span L there are therefore $L/l_y(\omega)$ uncorrelated sources along the span (taken to the nearest integer), each of which radiates to the far field upon interaction with the trailing edge. Consider now the coherence $\gamma^2_{p_s p_f}(\omega)$ between the surface pressure p_s at a point close to the trailing edge and the acoustic pressure p_f at a single far field location, defined by,

$$\gamma^2_{p_s p_f}(\omega) = \frac{|S_{p_s p_f}(\omega)|^2}{S_{p_s p_s}(\omega) S_{p_f p_f}(\omega)} \tag{1}$$

where $S_{p_s p_f}(\omega)$ is the cross spectral density between the surface pressure $p_s(\omega)$ and far field pressure $p_f(\omega)$ and where $S_{p_s p_s}(\omega)$ and $S_{p_f p_f}(\omega)$ are the auto-spectral densities of the surface pressure and far field pressures respectively. The far field pressure $p_f(\omega)$ is the sum of $L/l_y(\omega)$ statistically identical uncorrelated sources whose strength is proportional to the surface pressure $p_s(\omega)$ close to the trailing edge, each of which radiates to a far field observer with a near-identical transfer function $G(\omega)$. At a single frequency, therefore, the radiated pressure $p_f(\omega)$ may be related to the surface pressure $p_s(\omega)$ by

$$p_f(\omega) = \frac{L}{l_y(\omega)} G(\omega) p_s(\omega) \tag{2}$$

However, since the pressures are random, we consider the spectral density of the radiated pressure, $S_{p_f p_f}(\omega) = E\{p_f(\omega) p_f^*(\omega)\}$. Substituting Eq. 2 into this expression and assuming that each of the $L/l_y(\omega)$ sources $p_s(\omega)$ are mutually uncorrelated, gives

$$\begin{aligned} S_{p_f p_f} = E\{p_f(\omega) p_f^*(\omega)\} &= \sum_{n=1}^{L/l_y(\omega)} \sum_{n'=1}^{L/l_y(\omega)} E\{p_s(\omega, r_n) p_s^*(\omega, r_{n'})\} G(\omega, r_n) G^*(\omega, r_{n'}) \\ &= \frac{L}{l_y(\omega)} |G(\omega)|^2 S_{p_s p_s}(\omega) \end{aligned} \tag{3}$$

where $|G(\omega)|$ represents the value of $G(\omega, r_n)$ averaged over r_n and $S_{p_s p_s}(\omega) = E\{p_s(\omega, r_n) p_s^*(\omega, r_n)\}$ is the surface pressure auto-spectral density. This result simply

says that the overall mean square radiated pressure is the sum of $L/l_y(\omega)$ identical uncorrelated radiated pressures on the surface and is entirely consistent with classical result due to Amiet except that his expression includes the factor $Ll_y(\omega)$ as a result of double-integration along the span and the use of a different radiation function.

Similarly, substituting Eq. 2 into the expression for the cross power spectral density $S_{p_s p_f}(\omega) = E\{p_s(\omega)p_f^*(\omega)\}$ gives

$$S_{p_s p_f}(\omega) = \overline{G(\omega)} S_{p_s p_s}(\omega) \tag{4}$$

Substituting eqs. (3) and (4) in the Eq. 1 for the coherence yields,

$$\gamma^2_{p_s p_f}(\omega) = \left(\frac{l_y(\omega)}{L}\right)^2 \tag{5}$$

Clearly, therefore, the coherence between the surface pressure and far field pressure is unity when the surface pressure is fully coherent across the span. Equation 5 provides a simple and obvious interpretation of the coherence function as being equivalent to the number of uncorrelated sources. It also provides a means of estimating the coherence length from the near field / far-field coherence function,

$$l_y(\omega) = L\sqrt{\gamma^2_{p_s p_f}(\omega)} \tag{6}$$

The 'humps' in the coherence spectrum of relatively high coherence in these figures are therefore indicative of strong 'two-dimensionality' of the flow structure as might be expected from laminar separated flow.

F. Simultaneous far field noise and surface pressure measurement on pressure side

Figure 9 b) (right) shows the coherence spectra between a single far field receiver position and a point on the surface near the trailing edge (5 mm upstream) but now measured on the pressure side where there is no flow separation. The same peak frequencies as in Figure 9 a) can be observed but with generally higher coherence levels. This observation provides evidence for scattering at the trailing edge of the separated flow which affects both the suction and pressure sides. The reason for the generally higher coherence between the far field microphone and the pressure-side pressure,

compared to the suction side, is because the pressure side is not contaminated by non-radiating hydrodynamic pressure fluctuations which mostly occur on the suction side.

Confirmation of the higher levels of hydrodynamic pressure on the suction side is shown in Figures 10 a and b which show a direct comparison between the auto-spectral densities of the surface pressures on the pressure side and the suction side at the two angles of attack of $\alpha_{eff} = 10^{\circ}$ and $\alpha_{eff} = 14^{\circ}$. These two angles of attack correspond to the onset of separation at the trailing edge and leading edge respectively. The auto-spectral densities of the unsteady surface pressure are integrated over a bin width of 4.9 Hz. At $\alpha_{eff} = 10^{\circ}$ the suction-side surface pressure exceeds the pressure side by nearly 15 dB in the frequency range where separation noise is dominant. At the higher angle of attack, $\alpha_{eff} = 14^{\circ}$, where the flow is completely separated, the pressures on both sides of the aerofoil are roughly similar in the low frequency bandwidth where separation noise is dominant. This may be due to very long wavelengths (>1 m) associated with the noise due to flow separation in this case, which will diffract around the trailing edge causing both sides of the aerofoil to be similar.

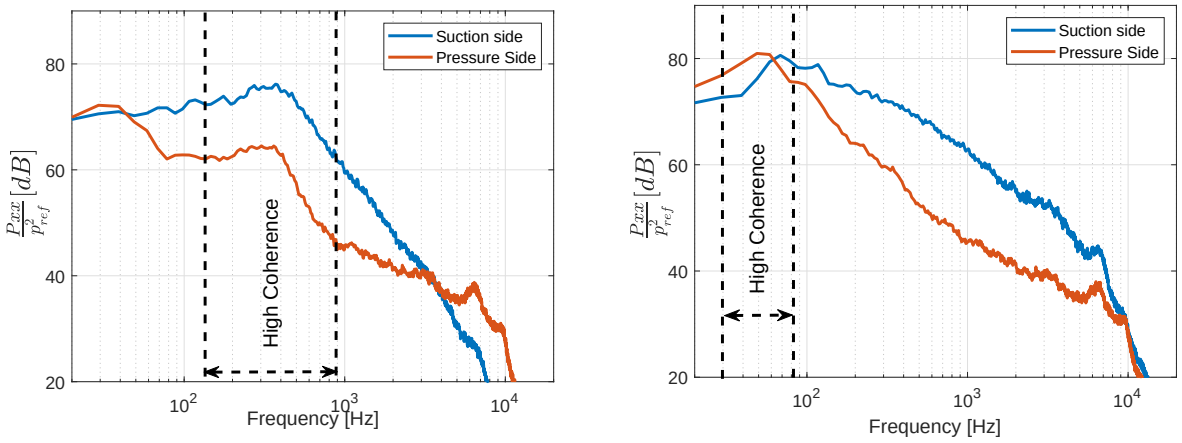

(a) $\alpha_{eff} = 10^{\circ}$ (b) $\alpha_{eff} = 14^{\circ}$

FIG. 10: Auto-spectral density of the unsteady surface pressure field at the TE on both sides of the aerofoil at a) $\alpha_{eff} = 10^{\circ}$ b) $\alpha_{eff} = 14^{\circ}$.

G. Comparison of surface and far field pressure spectra

Further demonstration of the causal link between the unsteady surface pressure close to the aerofoil trailing edge and the far field noise for separated flows can be obtained by simply compar-

ing their *increase* in spectra levels for various angles of attack above the spectrum at $\alpha_{eff} = 0^\circ$. The auto-spectral densities of far field noise and unsteady surface pressure are both integrated over a bin width of 4.9 Hz.

These comparisons between the surface pressure at the pressure tap closest to the trailing edge (5 mm upstream) and the microphone 90° to the trailing edge are shown in Figure 11 for the four representative angles of attack $\alpha_{eff} = 3^\circ; 10^\circ; 16^\circ; 23^\circ$. At $(\alpha_{eff} = 3^\circ)$ where the flow is attached, the increase in ΔPSD above the spectra at 0° is generally less than 5dB in both surface and far field spectra. At $\alpha_{eff} = 10^\circ$ as the flow separates at the aerofoil trailing edge the two plots exhibit strong similarity in the frequency range associated with separation noise ($f \approx 10^2 - 10^3$), clearly establishing the link between them. At $\alpha_{eff} = 16^\circ$ even though the flow is fully separated over the aerofoil surface the spectral shapes are similar within and beyond the frequency range where the coherence is high, again suggesting a causal link between them. However, at the much higher angle of $(\alpha_{eff} = 23^\circ)$ spectral shapes only match over a very narrow low frequency range with very poor agreement occurring at higher frequencies. This suggests that additional sources are likely to be present, other than at the trailing edge, at this high angle of attack.

By way of summary, therefore, the peak in the noise radiation spectrum characteristic of separation noise has two contributions:

1. A spectral peak in the surface pressure spectrum, whose origin will be investigated in section V J.

2. An increase in the coherence length in the same narrow frequency band, leading to an increase in radiation efficiency of the hydrodynamic pressure fluctuations near the trailing edge.

H. Velocity fields

In this section we attempt to identify the sources of separation noise through measurements of the unsteady flow around the aerofoil. Time-Resolved PIV was used to quantify the unsteady velocity field at a freestream velocity 20 m/s at an effective angle of attack of $\alpha_{eff} \approx 11^\circ$ corresponding to the condition at which trailing edge separation is well established. The maximum velocity was limited to 20 m/s due to constraints in the PIV setup. The Reynolds number is therefore not invariant to the noise measurements, anyhow we assume that the flow field is not strongly

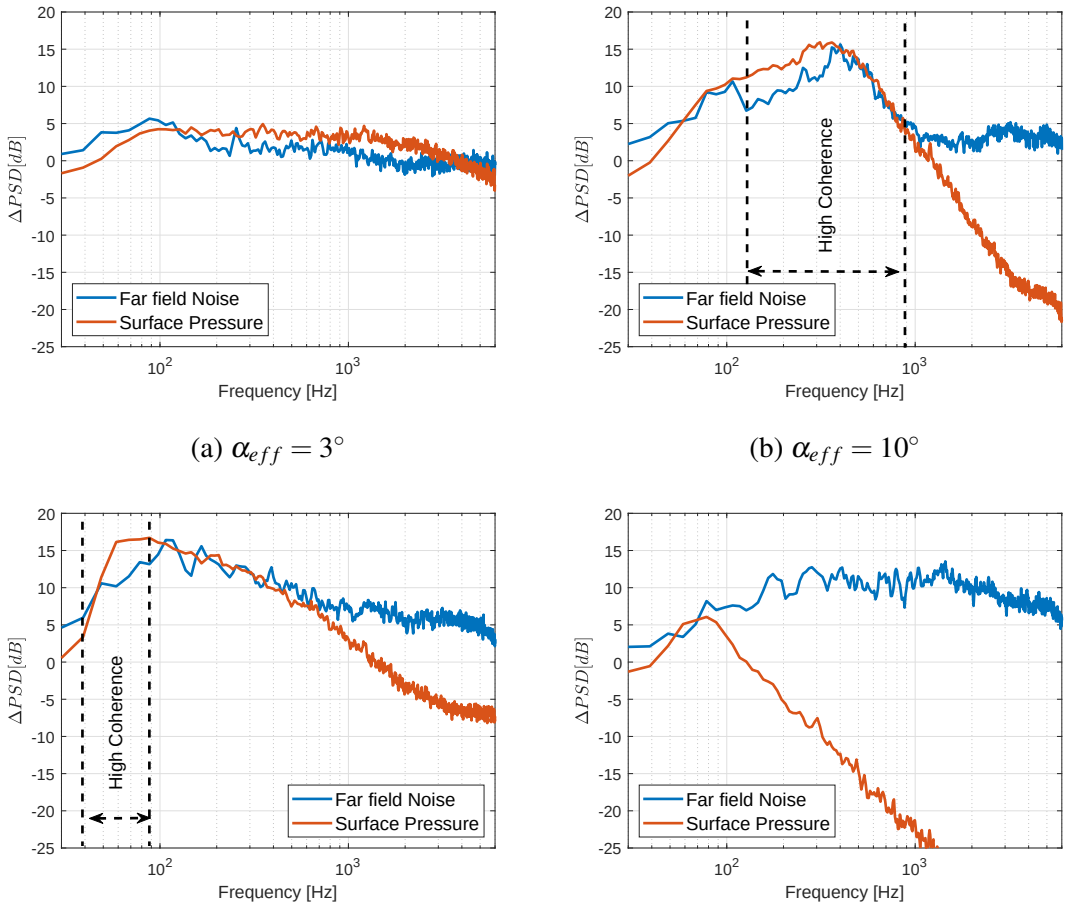

(a) $\alpha_{eff} = 3°$ (b) $\alpha_{eff} = 10°$

(c) $\alpha_{eff} = 16°$ (d) $\alpha_{eff} = 23°$

FIG. 11: Increase of the unsteady surface pressure at TE and far field noise auto-spectral densities above the spectrum at $\alpha_{eff} = 0°$ at a) $\alpha_{eff} = 3°$; b) $\alpha_{eff} = 10°$; c) $\alpha_{eff} = 16°$; d) $\alpha_{eff} = 23°$. $U_\infty = 40$ m/s.

affected by this dissimilarity even in terms of transition to a turbulent behaviour since the critical Reynolds number is well established to be above $Re \approx 5 \cdot 10^5$ [43]. Figures 12 a and 12 b show the contours of mean axial and transverse velocity components while figures 12 c and d show their corresponding root mean square (rms) values. The Reynolds shear stress and spanwise vorticity are plotted in figures 12 e and f. The extent of flow separation is evident in the plots of mean flow where separation can be seen to occur at about 60% of the chord from the trailing edge. High levels of fluctuating velocity and vorticity identify the shear layer and the main sources of unsteadiness that can provide the source of noise.

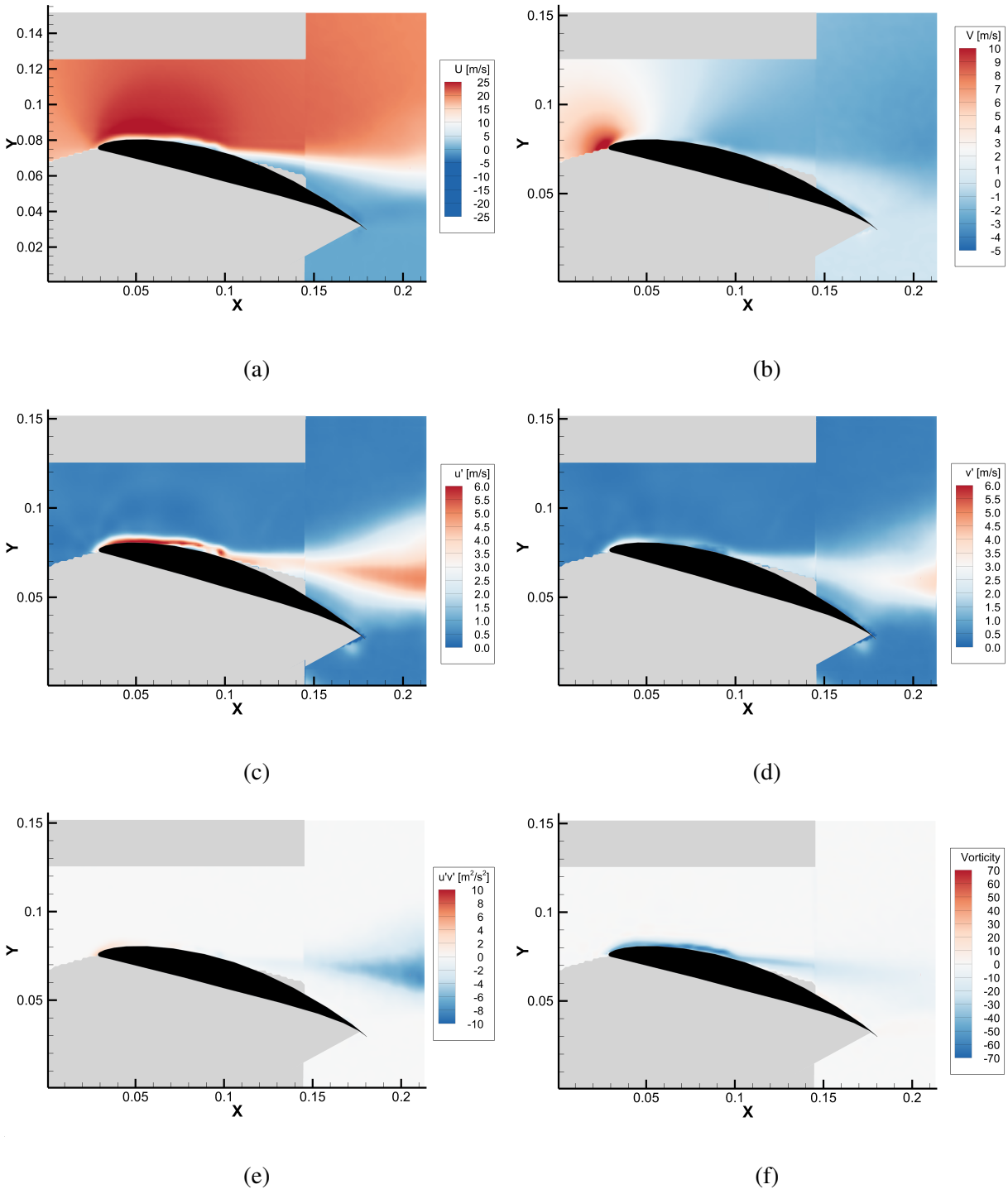

FIG. 12: Statistical description of the velocity field around the aerofoil. (a) Mean streamwise velocity U; (b) Mean vertical velocity V; (c) Streamwise velocity fluctuations u'; (d) Streamwise velocity fluctuations v'; (e) Reynolds stress $(u'v')$; (f) Mean spanwise vorticity $\omega_z = v_x - u_y$ normalized by U_∞/c. The units follow the SI metric system.

I. Causal relationship between boundary layer velocity fluctuations and unsteady surface pressure measurements

Previous sections have established the trailing edge as the origin of the radiated noise due to separated flow. We now attempt to identify the sources of turbulence in the separated flow that are responsible for the unsteady pressure close to the trailing edge in the narrow frequency bandwidth in which separation noise dominates. Here, we exploit the finding that separation noise occurs in a relatively small frequency bandwidth and must therefore be generated by reasonably coherent flow structures in the shear layer passing over the trailing edge. We therefore attempt to identify the sources of turbulent flow based on the assumption that they have maximum coherence with the surface pressure fluctuations near the trailing edge.

Surface pressure measurements 5 mm from the trailing edge were therefore made simultaneously with hot wire measurements of the streamwise velocity component at the aerofoil trailing edge, as shown in the schematic diagram and photograph of the measurement in Figures 13 a and b respectively. Hot wire measurements were made at 40 to 50 vertical positions in increments of 1.25 mm varying from 2 mm from the aerofoil surface to the free stream region. The procedure was repeated for the three effective angles of attack of $\alpha_{eff} \approx 11°$, $13°$ and $14°$, which encompasses regions II and III identified in Section V C, ranging between developing separation to fully separated flow, at $U_\infty = 20m/s$.

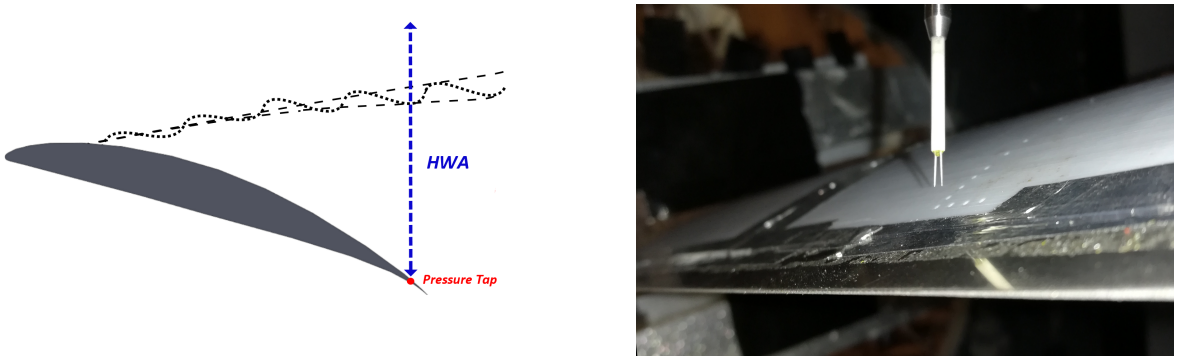

(a) (b)

FIG. 13: Sketch and photo of the implementation of the simultaneous measurement of velocity (by means of Hot Wire Anemometry (HWA)) and surface pressure

In figure 14, the variation in root mean square (rms) streamwise velocity with vertical height above the aerofoil is shown at different angles of attack. The height of maximum rms velocity

identifies the elevation of the shear layer, which divides the separated flow area from the free stream. As the angle of attack increases the height of the shear layer can be observed to move away from the aerofoil surface. Small oscillations in the velocity profiles can be observed with a period of about 5 mm. These features were found consistently on data obtained on different dates and aerofoils. So far the reasons for these oscillations are not clear and further work is needed to establish their cause.

Figure 15 a, b and c show colour contour maps of the coherence between the unsteady Hot Wire velocity data and the surface pressure, versus frequency and height above the surface at the trailing edge. The results are shown at the three angles of attack of 11°, 13° and 14° respectively. Again we associate the regions in the shear layer of high coherence (above 0.1) as being the sources responsible for the surface pressure fluctuations near the trailing edge and hence the far field noise.

In Figure 15 a) corresponding to $\alpha_{eff} \approx 11^\circ$ at least three distinct frequency regions of high coherence, and hence sources, can be identified. The region of most intense coherence with values above 0.5 occurs in the frequency range 10 Hz to 20 Hz and is present at all positions above the shear layer. By virtue of the low frequency and spatial extent of this region we speculate that this is due to flapping of the shear layer. The Strouhal number $St = \frac{f\,c\,sin(\alpha)}{U_\infty}$ of this region based on the projected width obstructing the flow is close to St = 0.03, which has previously associated with flapping shear layers for incipient separation conditions ([18, 19]), assuming a

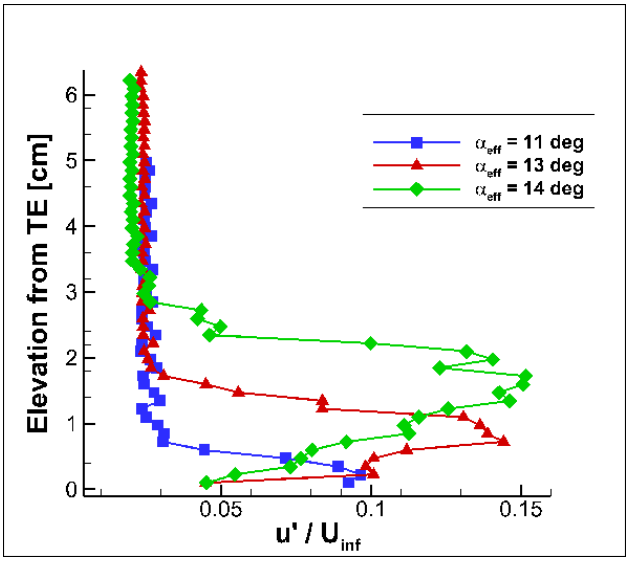

FIG. 14: Vertical profile of the standard deviation of the streamwise velocity component u' over the aerofoil trailing edge at different angles of attack and at $U_\infty = 20$ m/s

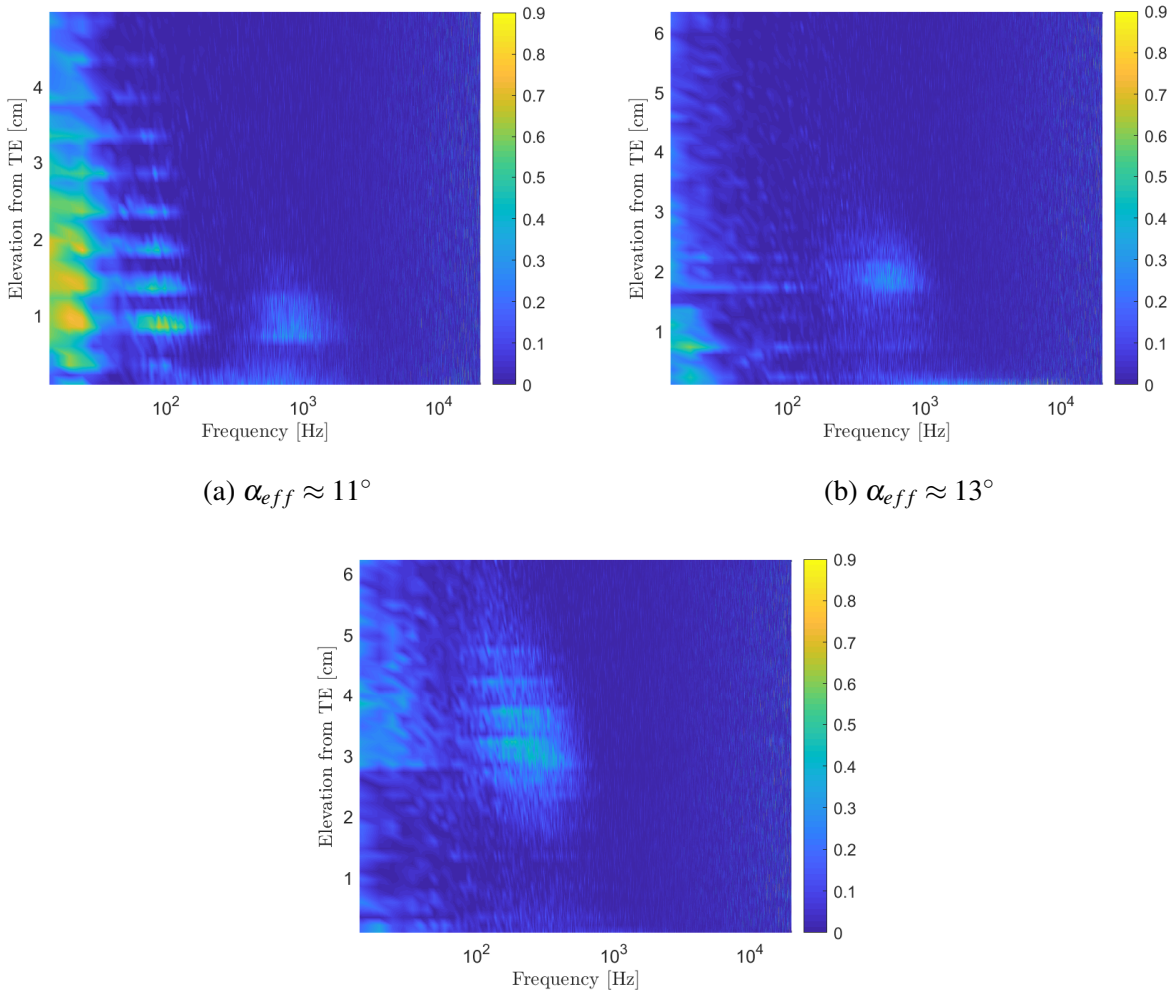

(a) $\alpha_{eff} \approx 11^\circ$

(b) $\alpha_{eff} \approx 13^\circ$

(c) $\alpha_{eff} \approx 14^\circ$

FIG. 15: Magnitude squared coherence between velocity and surface pressure at the trailing edge as a function of frequency and spatial location (vertical distance from the aerofoil surface) at $U_\infty = 20$ m/s: (a) $\alpha_{eff} \approx 11^\circ$; (b) $\alpha_{eff} \approx 13^\circ$; (c) $\alpha_{eff} \approx 14^\circ$;

"turbulent" boundary layer (and a value St = 0.02 for a laminar boundary). The flapping has been linked to a periodic switching between stalled and unstalled states on the upper aerofoil surface near the leading edge [19]. This low frequency flapping motion generates hydrodynamic pressure fluctuations that are present throughout the flow and on the aerofoil surface.

The second most intense region of high coherence in Figure 15 a occurs at frequencies close to 150 Hz, which is also distributed through the shear layer. The third much weaker source occurs at frequencies around 1000 Hz and is concentrated just above the shear layer. In section V J 1 below, PIV data for this angle of attack will be analysed in detail to extract the dominant flow structures

at these frequencies.

Increasing the angle of attack to $\alpha_{eff} \approx 13^{\circ}$ and $\alpha_{eff} \approx 14^{\circ}$ causes the source at 150 Hz to become weaker, while the high frequency source shifts towards lower frequencies and move further away from the surface.

J. Identification of the phenomena associated to separation noise

The previous section has shown that separation noise may be associated with a number of distinctive regions within the shear layer of different characteristic frequencies. In this section Dynamic Mode Decomposition is applied to the instantaneous velocity fields in order to identify the dominant flow 'structures' and associated frequencies in the PIV data at $\alpha_{eff} \approx 11^{\circ}$ that most closely correspond to the dominant frequencies observed in Figures 15.

1. Dynamic Mode Decomposition

Dynamic Mode Decomposition (DMD) is a common tool to identify and extract physically important features from experimental or numerical flow field data. This technique was first described in [44] and explained more fully by Schmid in [45]. The technique decomposes time-resolved flow field data into Koopman modes [46], each of which is associated with a single characteristic frequency and growth/decay rate. It makes the use of the instantaneous flow field measurements at K equispaced (Δt) instances in time (referred to as the *temporal dimension*). These snapshots are arranged into vectors $v(t_k) \equiv v_k$, whose *spatial dimension J* corresponds to the number of grid-points at which the velocity components are measured (for two dimensional data $J = 2(n_x \times n_y)$)), and then used to construct a *snapshot matrix*.

$$V_1^K = [v_1, v_2, ..., v_k, v_{k+1}, ..., v_{K-1}, v_K]$$

The output of the DMD is a Fourier-like expansion of the velocity field in terms of spatial modes in the form

$$v_k \approx v_k^{DMD} \equiv \sum_{m=1}^{M} a_m u_m e^{(\delta_m + i\omega_m)(k-1)\Delta t} \tag{7}$$

for k=1,....,K

Where u_m is the m^{th} DMD mode amongst the total of M modes, M being referred to as the *spectral complexity*, and a_m, δ_m and ω_m are the associated amplitudes, growth rates and frequencies. The dimension N of the vector subspace, generated by the M DMD modes and containing the approximation (7), is the *spatial complexity* which is $N \leq min(J,M)$.

The standard DMD algorithm is based on the *"Koopman assumption"* that a linear mapping **A** connects each snapshot v_k with the subsequent v_{k+1}:

$$v_{k+1} = \boldsymbol{A} v_k \tag{8}$$

for k=1,....,K-1

The DMD complex frequencies $\delta_m + i\omega_m$ and mode shape functions u_m are defined as the eigenvalues and eigenvectors of **A**. Since it is common that the number of snapshots is smaller than the number of grid-points of each snapshot $(K \ll J)$, it is not efficient to compute **A** explicitly, therefore a truncated Singular Value Decomposition SVD is usually applied to the snapshot matrix to reduce the order of the snapshot matrix and eliminate noise. The SVD is of the form:

$$V^k \simeq W \Sigma T^T \tag{9}$$

where $W^T W = T^T T = I$ where I is the unit matrix, W and T are the left and right eigenvectors, Σ is the diagonal matrix containing the singular values $\sigma_1, ..., \sigma_K$.

The reduced linear mapping matrix $\tilde{A}$ is defined as,

$$\tilde{A} = W_r^T A W_r \tag{10}$$

where W_r, Σ_r and T_r represent truncated approximations to W, Σ and T with small singular values removed. The reduced mapping matrix $\tilde{A}$ can therefore be obtained from the relation $V^{k+1} = \tilde{A} V^k$, substituting 9 and by post-multiplication by $T_r \Sigma_r^{-1} W_r^T$, which gives:

$$\tilde{A} = V^{K+1} T_r \Sigma_r^{-1} W_r^T \tag{11}$$

The mode shape functions and corresponding complex DMD eigenvalues are finally obtained from non-zero eigenvalues μ_m and eigenvectors $\tilde{q_m}$ of $\tilde{A}$ using the expression,

$$\tilde{A} \tilde{q_m} = \mu_m \tilde{q_m} \tag{12}$$

Finally, the growth rates δ_m and frequencies ω_m are associated with the eigenvalues μ_m through:

$$\delta_m + i\omega_m = log(\mu_m)/\Delta t$$

In this paper we use a recent extension of DMD, the *Higher Order DMD (HODMD)*, [47, 48] which is favourable in highly noisy complex flows. This method is able to independently clean the data from noise in both spatial and temporal directions and relies on two dimension-reduction steps, based on truncated SVD with a set tolerance on the SVD error, prior to the computation of the DMD modes and eigenvalues. The underlying assumption is a more general *"higher order Koopman assumption"* that relates each snapshot with d previous snapshots via some linear operators A_k as

$$v_{k+d} \simeq A_1 v_k + A_2 v_{k+1} + ... + A_d v_{k+d-1}$$

for $k = 1, ..., K-d$

Further details about the algorithm can be found in [48].

Figures 16 a, b and c show the decay rate (real part), amplitude and the ratio decay rate/amplitude (DA ratio) versus modal frequencies (imaginary part) respectively. These were obtained from the Higher Order DMD, applied to 1000 instantaneous snapshots. The latter figure shows a newly defined quantity that is useful in identifying the most significant modes associated with simultaneously low decay rate and high amplitude. Note that a small value of this ratio is an indicator of a possibly significant mode in the reconstruction of the time varying flow field.

Figures 16 reveal about 20 discrete modes over the frequencies between 0 and 2000 Hz (Nyquist frequency). No clear dominant modes can be observed which is consistent with the generally broadband character of the noise spectrum since no distinct dominant frequencies can be observed. We have therefore decided to investigate from the DMD spectrum the modes having an associated frequency close to the frequencies of high coherence between surface pressure, far field pressure and streamwise velocity, trying to identify any distinctive feature associated to these frequencies. The selected modes are highlighted by an arrow in figure 16 corresponding to the frequencies, $f = 16\ Hz$; $f = 143\ Hz$ and $f \approx 1\ kHz$. Since in Figure 15, the region of high coherence at high frequency has a relatively large frequency bandwidth, we have selected four modes to represent this source. We now describe each mode and examine its relationship to the frequencies at which high coherence between surface pressure and velocity are observed.

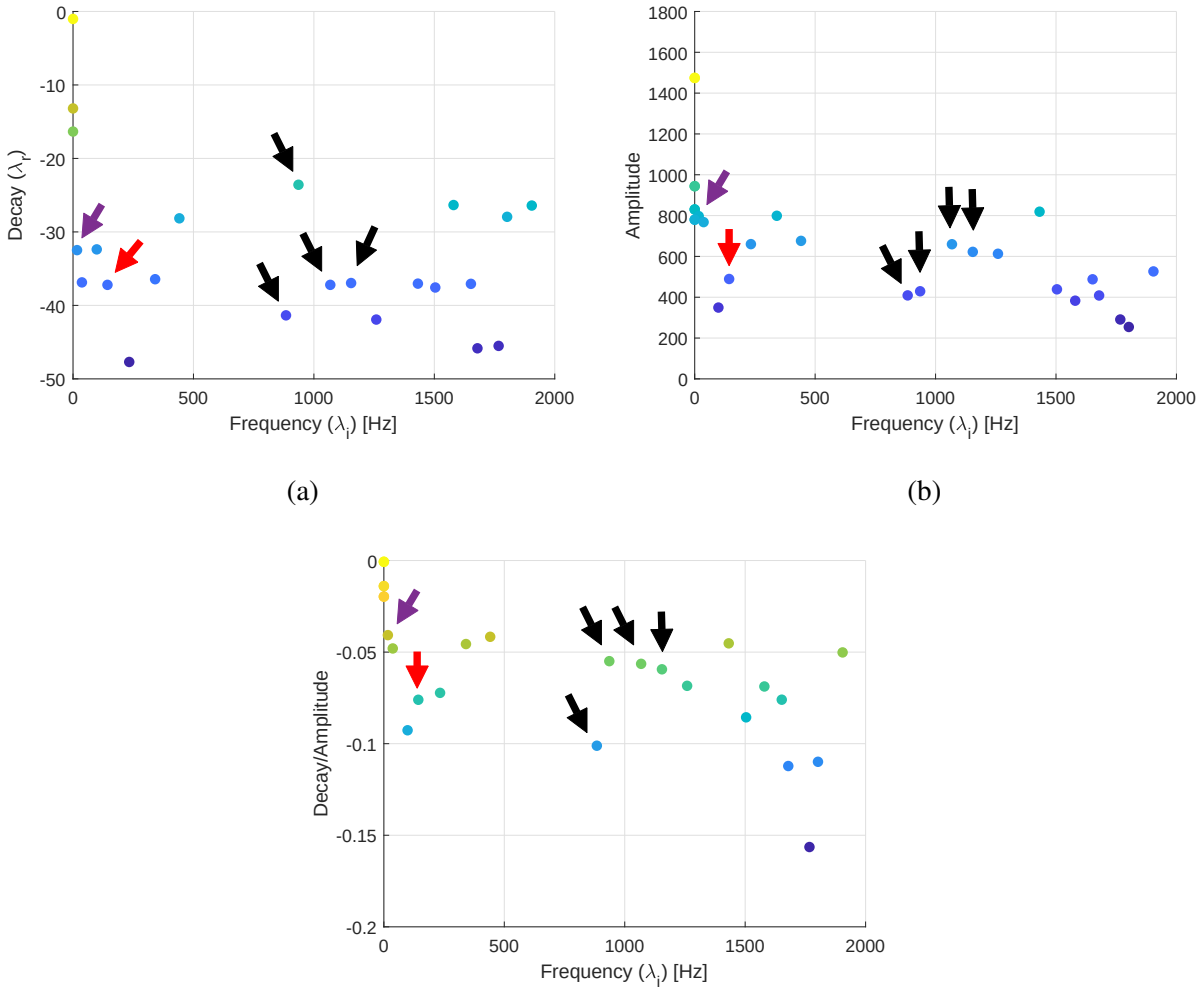

FIG. 16: DMD spectrum (a), amplitude absolute values (b) and ratio decay/amplitude (c) of the HODMD modes. $U_\infty = 20$ m/s; TRPIV sampling frequency $f_s = 4kHz$. The colorscale of the data points is a function of the relevance of the mode being a lighter colour more relevant than a darker. The arrows highlight the modes that are examined below in more detail.

The first mode (indicated by the purple arrow in figure 16), having an associated frequency f = 16 Hz, has a relatively low decay rate and significant amplitude, corresponding to a low DA ratio. This mode is therefore persistent and contributes significantly to the reconstruction of the overall flow field. As discussed above, this frequency is consistent with the Strouhal number associated with flapping of the shear layer in conditions of incipient separation. The DMD modes of the streamwise and vertical velocity components associated with this frequency are shown in figure 17 a and b respectively. They consist of regions of alternating higher and lower streamwise

velocity above the shear layer, while the vertical velocity component depicts a recirculating flow across the shear itself. Figure 16 c shows the contour of the instantaneous vorticity overlaid with the velocity vectors. It identifies areas of high negative and positive vorticity, possibly induced by the flapping shear layer, which occurs both within the shear and well above it.

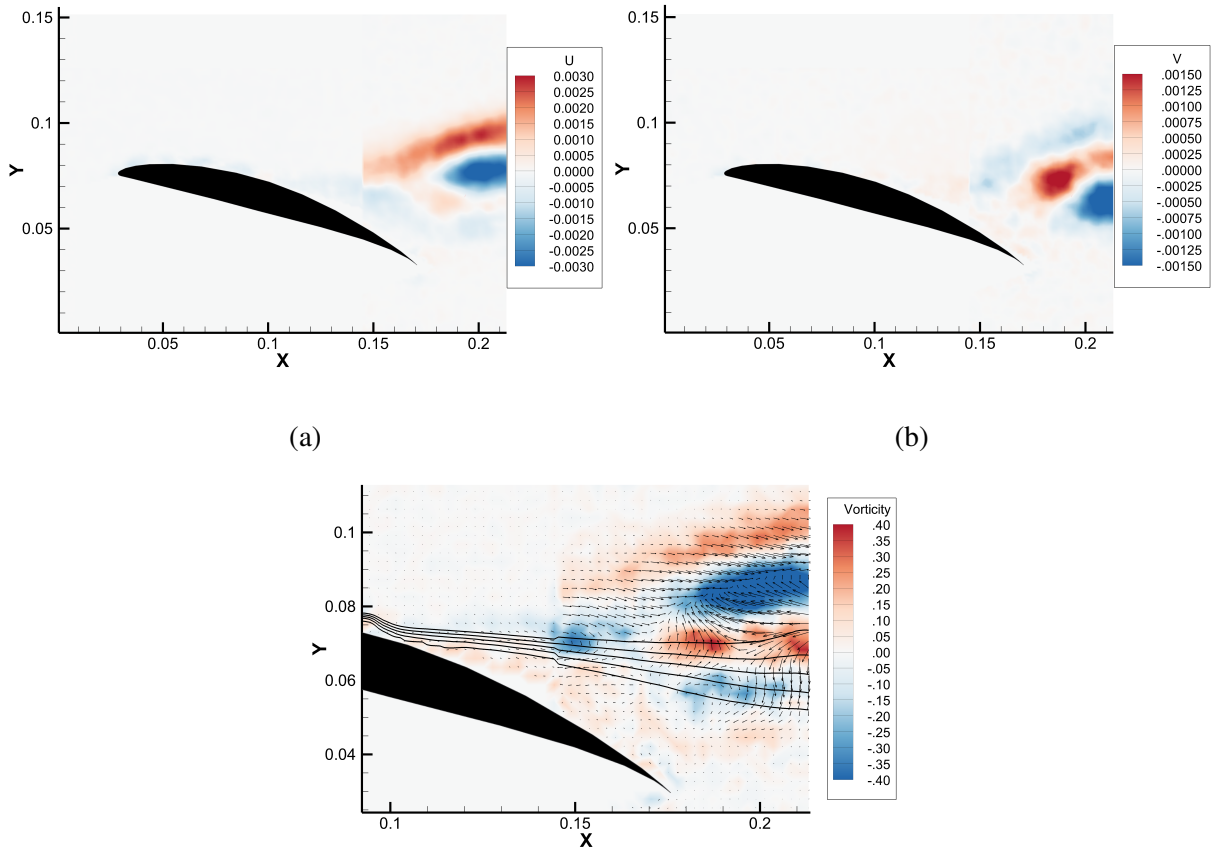

(a) (b)

(c)

FIG. 17: High Order DMD mode associated to the frequency f = 16 Hz (a) Streamwise U velocity component (b) Vertical V velocity component (c) Zoomed vorticity contour and velocity vectors with overlapped contour levels of the shear layer

The second DMD mode, indicated by the red arrow in the spectrum of figure 16, has frequency of 146 Hz, relatively low decay rate and slightly lower velocity amplitude, corresponding to a mid-value DA ratio. As for the previous mode, this mode is also persistent. The streamwise and vertical velocity components of this mode are represented in figure 18 a and b. It can be seen to be characterized by a strong streamwise velocity component but the vertical component above the shear layer is in the direction towards the shear while on the other side it is moving away from

the shear layer. The resultant velocity vectors plotted in figure 18 c give the appearance of flow converging axially as it moves downstream. Also shown in the figure is the spanwise vorticity, which can be seen to be rotating clockwise in the shear layer with induced counter-vorticity above the shear layer.

The frequency of this mode of $f = 146\,Hz$ can be seen in figure 19 a to match the peak of the spectral hump in the far field noise spectrum and the frequency of high coherence between the surface pressure and the far field noise at $U_\infty = 20\,m/s$, plotted in figure 19 b. It is therefore evident that this mode has an important role in the noise generation.

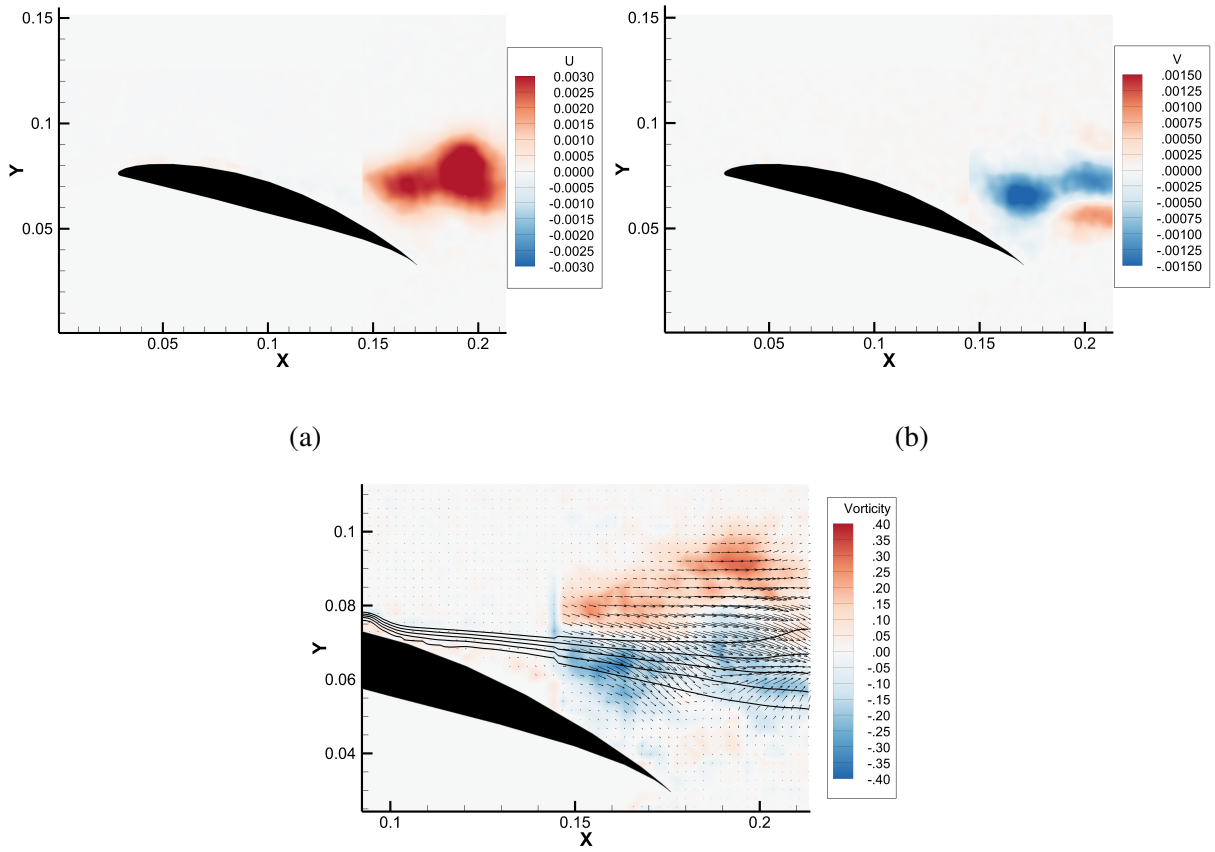

FIG. 18: High Order DMD mode associated to the frequency f = 143 Hz (a) Streamwise U velocity component (b) Vertical V velocity component (c) Zoomed vorticity contour and velocity vectors with overlapped contour levels of the shear layer

The coherence between streamwise velocity and surface pressure plotted in figure 15 shows a third region of relatively high coherence in the frequency range between $f \approx 0.8\,kHz$ and $f \approx$

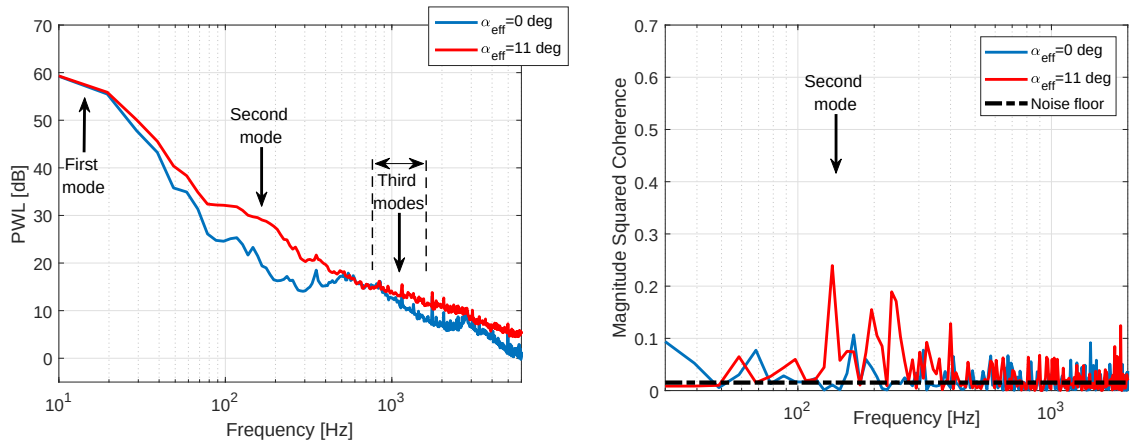

(a) (b)

FIG. 19: Sound Power Level (Left) and Coherence between far field noise and surface pressure on suction side (Right) at $\alpha_{eff} = 0^{\circ}$ and $\alpha_{eff} = 11^{\circ}$ at $U_{\infty} = 20/ : m/s$; The dashed line in b) represents the statistical noise floor.

1.3 kHz. However, unlike the first two regions, it is confined to a localised 1 cm region just above the shear layer. The DMD spectrum in figure 16 shows that there are at least four modes ($f = 884; 936; 1068; 1155\ Hz$) in this frequency band, all having a relatively low decay rate and mid to low amplitudes. The associated DA ratio is consequently low or mid/low. The flow fields associated with these four modes, which are depicted in figure 20, can be seen to differ in character. The first mode at $f = 884\ Hz$ figure 20 a indicates regions of alternating vorticity located inside the shear layer. The scale of these regions appear similar to the shear layer thickness of about 2 cm. Coherent vorticity of this scale convecting at $U = 20\ m/s$ will generate noise at a characteristic frequency $f \approx 20/0.02 = 1\ kHz$, which is entirely consistent with the modal frequency. The second mode with frequency $f = 936\ Hz$ in figure 20b shows evidence of fluid being ejected upwards and then convecting downstream with the flow. The third mode at $f = 1068\ Hz$ has similar character to the first mode. Finally, the fourth mode at a frequency of $f = 1155\ Hz$ is characterized by two elongated regions of opposite sign vorticity within and above the shear layer.

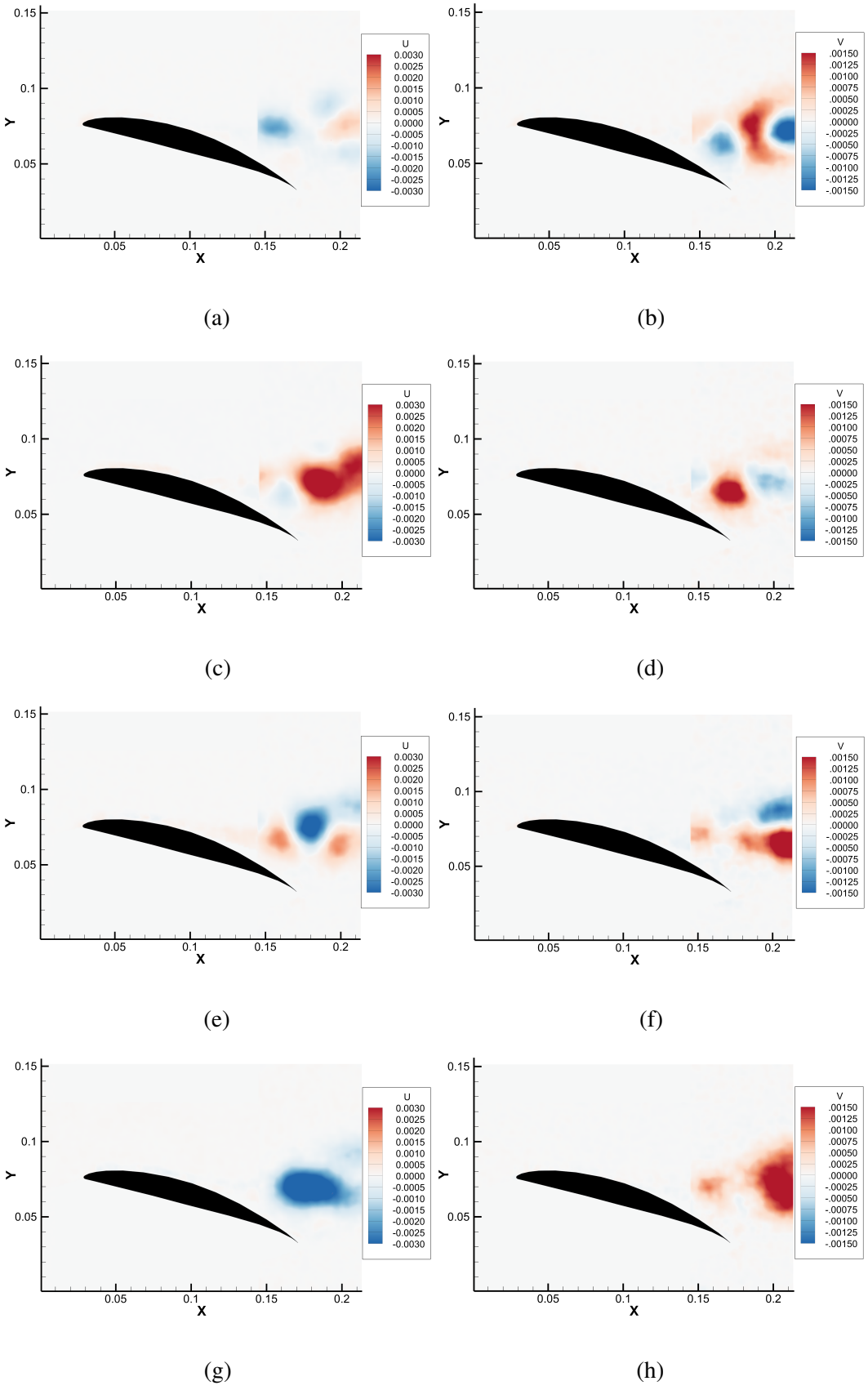

FIG. 20: High Order DMD modes: Left) Streamwise U velocity component Right) Vertical V velocity component (a)(b) f = 884 Hz; (c)(d) f= 936 Hz; (e)(f) f = 1068 Hz ; (g)(h) f= 1155 Hz

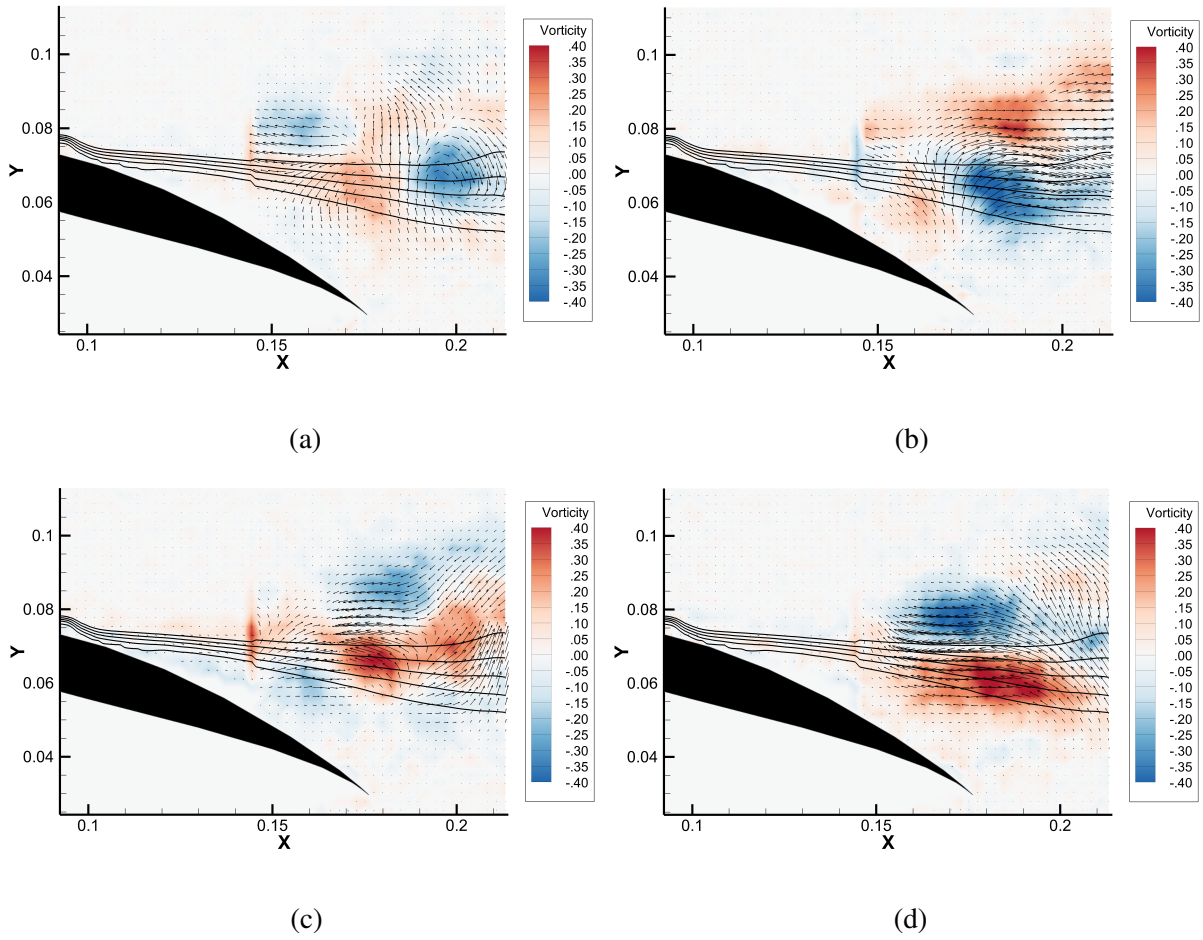

FIG. 21: High Order DMD modes: Zoomed vorticity contour and velocity vectors with overlapped contour levels of the shear layer: (a) f = 884 Hz; (b) f= 936 Hz; (c) f = 1068 Hz ; (d) f= 1155 Hz

VI. CONCLUSIONS

In this paper the sound generated by an aerofoil has been investigated experimentally over a wide range of angles of attack, including pre-stall and post-stall conditions. Detailed hot wire and PIV measurements of the unsteady velocity around the aerofoil were also made. In addition, static pressure measurements on both sides of the aerofoil were also performed to assess where flow separation has occurred. The unsteady surface pressure and velocity throughout the boundary layer and shear layer were measured simultaneously and analysis applied to determine the regions in the flow that were coherent with the surface pressure near the trailing edge, which was found to be responsible for far field radiation. Modal analysis on the PIV data was performed to extract the

dominant flow characteristics at the frequencies of maximum coherence between surface pressure and velocity.

The study concentrates on a NACA65-(12)10 aerofoil but most of the findings can be generalized to different aerofoils. The aim was understanding in more detail the generation mechanism of the so called *separation/stall noise*, being one of the possible self-noise sources of an aerofoil. An understanding of this mechanism may lead to approaches to mitigate this noise source.

The conclusions from this work may be summarized as follows:

- Three possible mechanisms have been identified to explain the noise generation due to an aerofoil close to stall. Flapping of the shear is a cause of very low frequency sound while the formation of coherent structures and instabilities in the shear layer have also been identified as possible noise sources for the separation/stall noise at low to mid frequencies. In all cases, these sources produce strong hydrodynamic pressure fluctuation close to the trailing edge which then scatter into sound.

- The noise spectrum due to aerofoil at varying angle of attack has been shown to fall into four categories. The first is at low angle of attack where the boundary layer is attached. Here the radiated noise spectrum is relatively broadband. The second occurs at angles of attack where the flow has partially separated. In this case the noise spectrum is characterized by a relatively narrow peak whose peak frequency reduces as angle of attack increases. The third identifies the condition of maximum overall noise radiation and occurs at the angle of attack where the flow just becomes fully separated such that the point of separation has reached the leading edge. At this condition the noise spectrum is in addition broadband. Finally, the fourth region occurs at post-stall angles of attack. Here, the noise spectrum becomes increasingly broadband as angle of attack increases but its overall level begins to reduce before increasing again due to a bluff body behaviour.

- Analysis has revealed the locations in the flow whose coherence between the unsteady surface pressure near the trailing edge and the local velocity is maximum. The analysis was undertaken for the aerofoil at 11° angle of attack, corresponding to second noise spectrum region defined above. These locations may be regarded as the sources of separation noise throughout the shear layer. Each of these sources occur over a particular frequency range and spatial region. Low frequency sources appear to be distributed over a large region above

the shear layer. At higher frequencies, however, the sources appear more localized but still above the shear layer.

- The velocity modes at the frequencies of maximum coherence were investigated through modal analysis of the PIV velocity data. The mode associated with the frequency hump of the noise spectrum was identified and shown to be characterized by a region of negative spanwise vorticity located entirely within the shear layer and similar size region above the shear of positive vorticity. The modes associated with the lower and higher frequency components of the spectrum were also identified.

ACKNOWLEDGMENTS

The authors would like to thank the financial support from the EPSRC Research Grant No: EP/N020413/1 on the "Quiet Aerofoils of the Next Generation" at the University of Southampton.

[1] T. F. Brooks, D. S. Pope, and M. A. Marcolini, Airfoil self-noise and prediction, NASA reference publication 1218 (1989).

[2] R. A. Wallis, Wind tunnel studies of leading edge separation phenomena on a quarter scale model of the outer panel of the handley page "victor" wing, with and without nose droop, Reports and Memoranda of the Aeronautical Research Council No. 3455 (1965).

[3] H. Schlichting and K. Gersten, *Boundary-layer theory* (Springer, 2016).

[4] R. Amiet, Noise due to turbulent flow past a trailing edge, Journal of sound and vibration **47**, 387 (1976).

[5] F. Bertagnolio, H. A. Madsen, A. Fischer, and C. Bak, A semi-empirical airfoil stall noise model based on surface pressure measurements, Journal of Sound and Vibration **387**, 127 (2017).

[6] M. Fink and D. Bailey, Airframe noise reduction studies and clean-airframe noise investigation, Final Report United Technologies Research Center, East Hartford, CT. (1980).

[7] R. W. Paterson, R. K. Amiet, and C. L. Munch, Isolated airfoil-tip vortex interaction noise, Journal of Aircraft **12**, 34 (1975).

[8] S. Moreau, M. Roger, and J. Christophe, Flow features and self-noise of airfoils near stall or in stall, AIAA paper **3198**, 2009 (2009).

[9] C. Y. Schuele and K.-S. S. Rossignol, Trailing-edge noise modeling and validation for separated flow conditions, in *19th AIAA/CEAS Aeroacoustics Conference* (2013) p. 2008.

[10] A. Suryadi and M. Herr, Wall pressure spectra on a DU96-W-180 profile from low to pre-stall angles of attack, in *21st AIAA/CEAS Aeroacoustics Conference* (2015) p. 2688.

[11] S. Yarusevych, P. E. Sullivan, and J. G. Kawall, Coherent structures in an airfoil boundary layer and wake at low Reynolds numbers, Physics of Fluids **18**, 044101 (2006).

[12] J. M. Lin and L. L. Pauley, Low-Reynolds-number separation on an airfoil, AIAA journal **34**, 1570 (1996).

[13] S. Yarusevych, P. E. Sullivan, and J. G. Kawall, On vortex shedding from an airfoil in low-Reynolds-number flows, Journal of Fluid Mechanics **632**, 245 (2009).

[14] S. Burgmann and W. Schröder, Investigation of the vortex induced unsteadiness of a separation bubble via time-resolved and scanning PIV measurements, Experiments in fluids **45**, 675 (2008).

[15] T. Berk, G. Lacagnina, C. Paruchuri, P. Joseph, and B. Ganapathisubramani, Simultaneous surface pressure and high-speed PIV measurements in stalled airfoil, in *19th International Symposium on Applications of Laser Techniques to Fluid Mechanics* (Instituto Superior Tecnico, 2018).

[16] J. H. Watmuff, Evolution of a wave packet into vortex loops in a laminar separation bubble, Journal of Fluid Mechanics **397**, 119 (1999).

[17] P. J. Shapiro, *The influence of sound upon laminar boundary layer instability*, Tech. Rep. (Massachusetts Inst of Tech Cambridge Acoustics and Vibration Lab, 1977).

[18] K. Zaman, A. Bar-Sever, and S. Mangalam, Effect of acoustic excitation on the flow over a low-re airfoil, Journal of Fluid Mechanics **182**, 127 (1987).

[19] K. Zaman, D. McKinzie, and C. Rumsey, A natural low-frequency oscillation of the flow over an airfoil near stalling conditions, Journal of Fluid Mechanics **202**, 403 (1989).

[20] I. H. Abbott and A. E. Von Doenhoff, *Theory of wing sections, including a summary of airfoil data* (Courier Corporation, 1959).

[21] T. Chong, P. Joseph, and P. Davies, Design and performance of an open jet wind tunnel for aero-acoustic measurement, Applied acoustics **70**, 605 (2009).

[22] T. Brooks, M. Marcolini, and D. Pope, Airfoil trailing edge flow measurements and comparison with theory, incorporating open wind tunnel corrections, in *9th Aeroacoustics Conference* (1984) p. 2266.

[23] C. E. Willert and M. Gharib, Digital particle image velocimetry, Experiments in fluids **10**, 181 (1991).

[24] M. Raffel, C. E. Willert, J. Kompenhans, *et al.*, *Particle image velocimetry: a practical guide* (Springer Science & Business Media, 2007).

[25] C. Cierpka, B. Lütke, and C. J. Kähler, Higher order multi-frame particle tracking velocimetry, Experiments in Fluids **54**, 1533 (2013).

[26] R. J. Adrian and J. Westerweel, *Particle image velocimetry*, 30 (Cambridge University Press, 2011).

[27] J. Soria, An investigation of the near wake of a circular cylinder using a video-based digital cross-correlation particle image velocimetry technique, Experimental Thermal and Fluid Science **12**, 221 (1996).

[28] F. Scarano, Iterative image deformation methods in PIV, Measurement science and technology **13**, R1 (2001).

[29] H. Huang, H. Fiedler, and J. Wang, Limitation and improvement of PIV, Experiments in fluids **15**, 263 (1993).

[30] K. Jambunathan, X. Ju, B. Dobbins, and S. Ashforth-Frost, An improved cross correlation technique for particle image velocimetry, Measurement Science and Technology **6**, 507 (1995).

[31] J. Nogueira, A. Lecuona, and P. Rodriguez, Local field correction PIV: on the increase of accuracy of digital PIV systems, Experiments in fluids **27**, 107 (1999).

[32] J. Westerweel and F. Scarano, Universal outlier detection for PIV data, Experiments in fluids **39**, 1096 (2005).

[33] M. Drela, Xfoil: An analysis and design system for low Reynolds number airfoils, in *Low Reynolds number aerodynamics* (Springer, 1989) pp. 1–12.

[34] I. Tani, Low-speed flows involving bubble separations, Progress in Aerospace Sciences **5**, 70 (1964).

[35] J. D. Anderson Jr, *Fundamentals of aerodynamics* (McGraw-Hill Education, 2010).

[36] S. Narayanan, P. Chaitanya, S. Haeri, P. Joseph, J. Kim, and C. Polacsek, Airfoil noise reductions through leading edge serrations, Physics of Fluids **27**, 025109 (2015).

[37] W. K. Blake, *Mechanics of flow-induced sound and vibration, Volume 2: Complex flow-structure interactions* (Academic press, 1986).

[38] R. Parchen, A prediction scheme for trailing edge noise based on detailed boundary layer characteristics, Progress report DRAW (1998).

[39] O. Stalnov, P. Chaitanya, and P. F. Joseph, Towards a non-empirical trailing edge noise prediction model, Journal of Sound and Vibration **372**, 50 (2016).

[40] R. E. Sheldahl and P. C. Klimas, *Aerodynamic characteristics of seven symmetrical airfoil sections through 180-degree angle of attack for use in aerodynamic analysis of vertical axis wind turbines*, Tech. Rep. (Sandia National Labs., Albuquerque, NM (USA), 1981).

[41] N. Gregory and C. O'Reilly, *Low-Speed aerodynamic characteristics of NACA 0012 aerofoil section, including the effects of upper-surface roughness simulating hoar frost* (HM Stationery Office London, 1973).

[42] D. E. Gault, A correlation of low-speed, airfoil-section stalling characteristics with Reynolds number and airfoil geometry, NACA Technical Note 3963 (1957).

[43] M. Brendel and T. J. Mueller, Boundary-layer measurements on an airfoil at low Reynolds numbers, Journal of aircraft **25**, 612 (1988).

[44] P. Schmid and J. Sesterhenn, Dynamic Mode Decomposition of numerical and experimental data, in *APS Division of Fluid Dynamics Meeting Abstracts* (2008) p. MR.007.

[45] P. J. Schmid, Dynamic mode decomposition of numerical and experimental data, Journal of fluid mechanics **656**, 5 (2010).

[46] B. O. Koopman, Hamiltonian systems and transformation in Hilbert space, Proceedings of the National Academy of Sciences **17**, 315 (1931).

[47] S. Le Clainche and J. M. Vega, Higher order dynamic mode decomposition, SIAM Journal on Applied Dynamical Systems **16**, 882 (2017).

[48] S. Le Clainche, J. M. Vega, and J. Soria, Higher order dynamic mode decomposition of noisy experimental data: the flow structure of a zero-net-mass-flux jet, Experimental Thermal and Fluid Science **88**, 336 (2017).